Chapter 1

Introduction

1.1. Present scenario of water pollution

Fresh water is the lifeblood of our planet, sustaining every living organism, fuelling ecosystems, and serving as the foundation for survival, growth, and prosperity. The search for life on Mars and other planets in the solar system and beyond often begins with a fundamental question: Does water exist there? The reason for asking this seemingly mundane question stems from the understanding that water symbolizes life. Water is essential for all life on Earth, directly or indirectly supporting every organism. It is present in every cell and tissue of animals and vital for metabolic processes and reproduction in many species [1, 2]. Scientific evidence suggests that life began in water and gradually expanded onto the land more than 400 million years ago [3]. Thus, the significance of water for sustaining life is undeniable. At present, Earth's water distribution is strikingly uneven, with 97.5% being saltwater and only 2.5% freshwater [4]. Of the total freshwater, 68.7% exists in the form of glaciers and ice caps (which are not accessible to humans in day to day life), 30.1% is stored in aquifers and underground, and a mere 1.2% is found in surface water bodies such as lakes, rivers, and the atmosphere (illustrated in Figure 1.1).

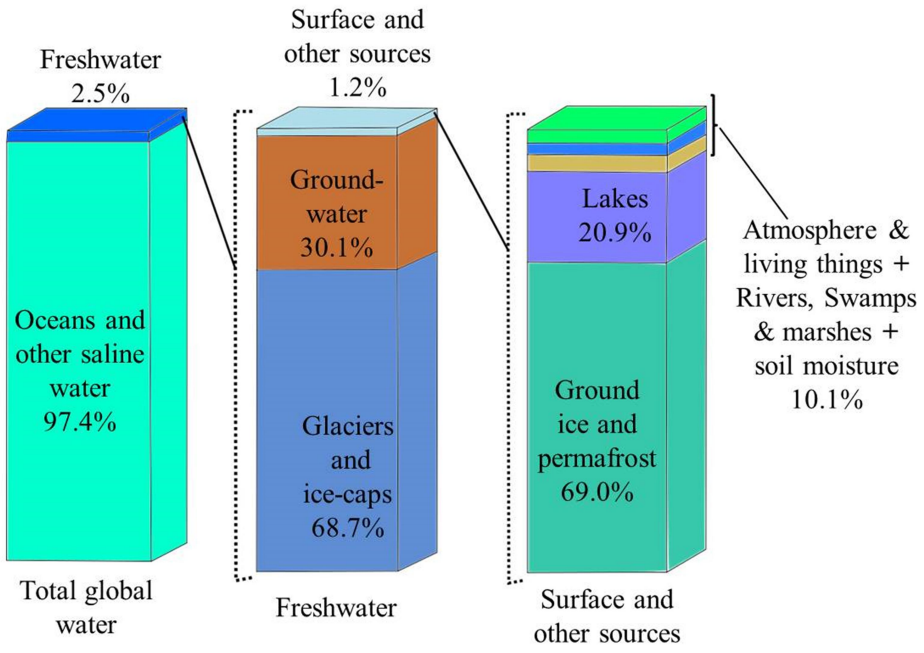

Figure 1.1. Water distribution on Earth [4].

Therefore, it is crucial that these scarce freshwater sources must be preserved and should be utilized judiciously and sustainably. On the contrary, freshwater sources are increasingly being depleted and contaminated due to rising industrial activities and the relentless pursuit of technological advancement [5, 6]. Water pollution poses a severe global threat, affecting both freshwater reserves and marine ecosystems, with its impact intensifying alongside rapid population growth [5, 7]. Major contributors include industrial discharges as well as domestic and municipal wastewater [5, 8]. In industries, contaminants originate from various manufacturing stages ranging from synthesis to processing and product formation. In urban cities, domestic and municipal discharge contain diverse organic and inorganic pollutants, including heavy metals, which deteriorate water quality.

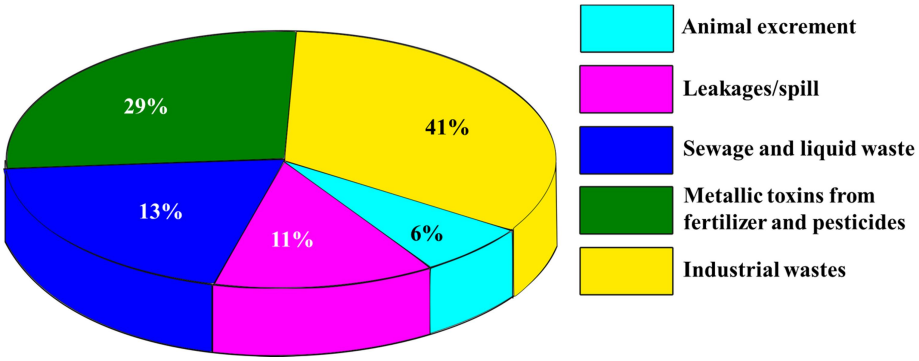

Figure 1.2. Pie chart representation of water pollution sources [9].

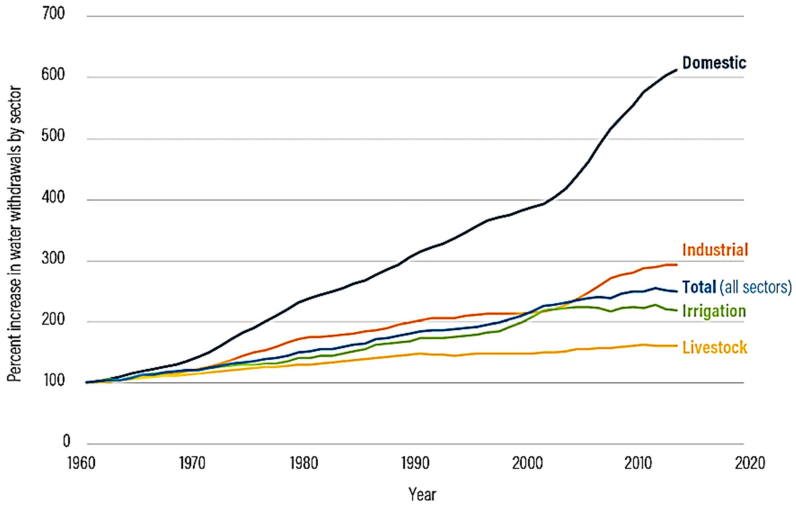

Figure 1.3. Graph showing the percentage increase in water usage across different sectors [10].

Figure 1.2 shows a pie chart showing the distribution of water pollution sources percentage wise [9]. The data reveals that industrial dumping is the leading source of water pollution, contributing around 41%**.** The water withdrawal over the world is only increasing as inferred from the data as shown in Figure 1.3 [10]. Therefore, for the sustainable use of water, wastewater must be properly treated before being discharged to natural water sources.

1.2. Wastewater treatment

A typical water treatment procedure follows a sequential treatment of wastewater in multiple stages. Initially preliminary treatment is done, followed by primary and secondary treatment as the second and third stages, and ends with the last treatment called tertiary treatment or advanced treatment (Figure 1.4). Preliminary treatment employs methods like screening, comminution, and grit removal to eliminate large debris and solids from wastewater [8]. In the next stage, primary treatment separates suspended solids, leftover grit, fats and oils using different methods such as filtration, sedimentation, coagulation, and floatation [5, 8]. Secondary treatment is then applied, in which biodegradable organics and nutrients, including nitrogen and phosphorus, are removed through biochemical reactions involving both aerobic and anaerobic processes [5, 8]. Finally, tertiary treatment employs advanced methods to purify the water to a level suitable for reuse or safe discharge for specific applications [8]. Few notable methods include adsorption, ion exchange, solvent extraction and reverse osmosis, all of which are quite effective in separating pollutant compounds from water by transferring them to a separate medium or reservoir. However, tertiary treatment methods have certain limitations, particularly when the removed pollutants are transformed into secondary pollutants that require additional treatment [5, 11]. For instance, while adsorption captures pollutants from water, regenerating the adsorbent and separating it from the adsorbate add both cost and complexity to the treatment process [11]. In the most recent development, belonging to the tertiary treatment method, advanced oxidation processes known as AOPs have gained much popularity as a superior pollutant removal technique. AOPs involve various chemical reactions that generate highly reactive species, such as hydroxyl radicals (**•**OH**)**, which targets the complex pollutant molecules, effectively mineralizing them into harmless compounds such as carbon dioxide, water, and mineral salts [12, 13]. AOPs are regarded as environmentally

friendly technologies. Among various AOPs such as ozonation, electrochemical oxidation, Fenton and Fenton-like processes, photocatalysis has emerged as one of the most favorable techniques, owing to its ability to utilize light (particularly solar energy) as a driving force to induce chemical reactions on the catalyst's surface and on its vicinity [14, 15]. These photocatalytic reactions can be deliberately utilized for the decomposition of the pollutants present in the water medium.

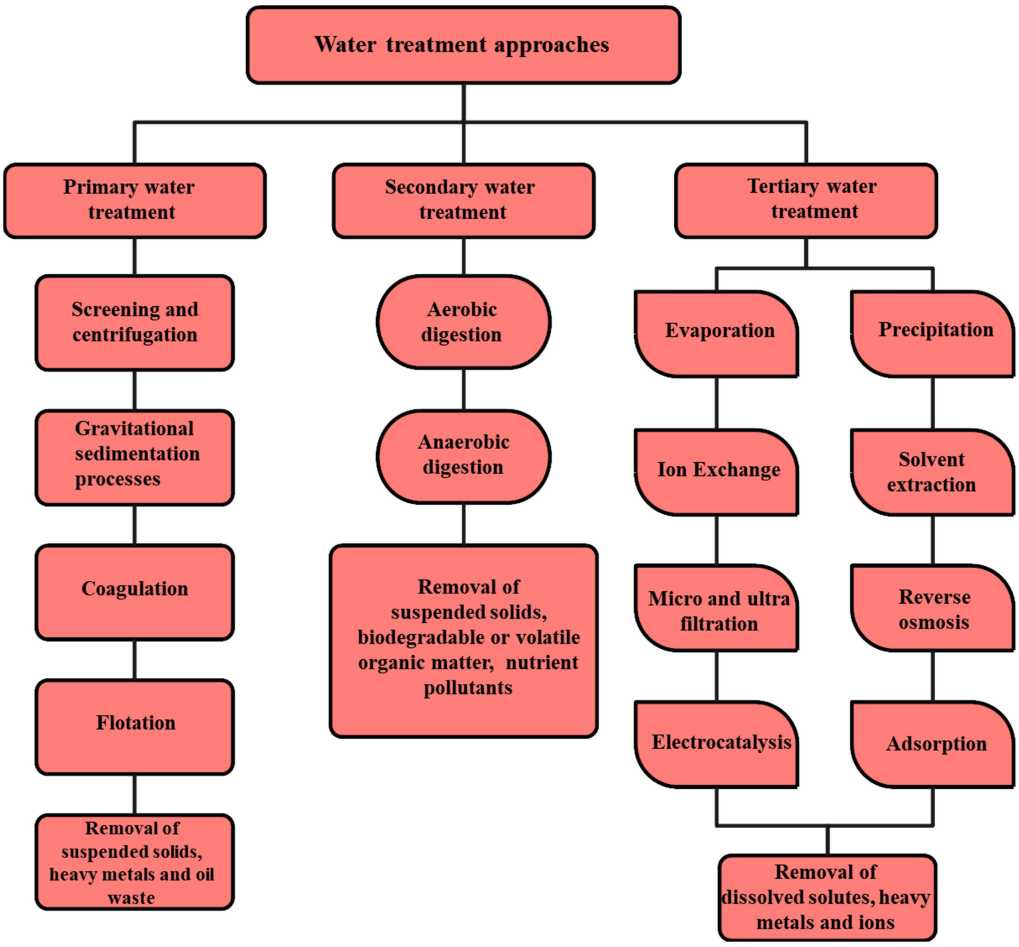

Figure 1.4. Classification of water purification techniques [5].

Dye pollutants originating from textile and other industries represent a major category of organic pollutants that contaminate the environment. It is estimated that there are as many as 10,000 unique synthetic dyes prevalent in the global market with production reaching over 700,000 ton annually [16]. Approximately 200,000 tons of dyes enter the environment annually due to inefficiencies in textile dyeing processes, with industrial wastewater statistics revealing that 17-20% of such waste originates from dyeing and

finishing activities [16]. This is alarming, as such wastewater carries a wide range of hazardous effects depending on the dye color and composition. For instance, the intense coloration of dyes can block sunlight from penetrating deep into aquatic ecosystems, disrupting aquatic life and ecological balance [12]. Azo dyes, a particular group of dyes with aromatic rings and characterized by the presence of one or more azo groups (-N=N-) are renowned for their harmful effects [12]. They are highly water-soluble and chemically stable, making them resistant to degradation, and persistent in the environment. They are known to be highly toxic, carcinogenic, and mutagenic. Also, the dye containing wastewater affect the vitality of the aquatic system with its pH effects, high biological oxygen demand (BOD) and chemical oxygen demand (COD). Some effects observed on human health from these wastewater include headache, nausea, skin irritation, lungs problem, and congenital malformation [16]. Therefore, it is crucial to treat these dyes before they are released into natural water bodies.

1.3. Photocatalysis

A catalyst is a substance whose presence in the reaction environment enhances the reaction rate, while itself remaining unchanged at the end of the reaction, i.e., its composition stays the same [17]. Correspondingly, catalysis is the process in which reactants undergo reaction in the presence of catalyst, under the condition that catalyst remains stable and reusable for another reaction. However, different specific definitions of catalysis have emerged and the one given by Serpone et al. is “catalysis refers simply to a process in which a substance (the catalyst) accelerates, through intimate interaction(s) with the reactant(s) and concomitantly providing a lower energy pathway, an otherwise thermodynamically favored but kinetically slow reaction with the catalyst fully regenerated quantitatively at the conclusion of the catalytic cycle” [18]. Evidently, involving catalysis, the term ‘photocatalysis’ is derived from two words: ‘photo’ and ‘catalysis’ [19]. However, the exact meaning of the term ‘photocatalysis’ has been a subject of debate, with Serpone et al. emphasizing that it should be simply understood as a catalysis involving two necessary entities: light and catalyst [18]. Without referring to a specific mechanism involved in the process, the term ‘photocatalysis' describes a process in which the catalyst accelerates the photoreaction. Depending upon the reaction mechanism, any of the following situation occurs : (i) the photoreaction is accelerated by the interaction of the catalyst and the substrate in its ground state, (ii) the catalyst

accelerates the photoreaction by interacting with the substrate in its excited state, (iii) the interaction of the catalyst with the light produces primary product which in turn interacts with substrate inclusively or exclusively of the situation as stated in (i) or (ii). Thus, the expression 'photocatalysis' is broad and encompasses all types of photoreactions including the process of photosensitization [18]. The photocatalysis that involves usage of solid metal oxide semiconductors such as TiO_2, Cu_2O, CuO, ZnO, NiO, WO_3, Fe_2O_3 as photocatalysts for degradation of organic pollutants (such as dyes) dissolved in a solution, is then better known as semiconductor-based heterogeneous photocatalysis [15, 18]. In this process, light irradiation of semiconductor leads to the generation of charge carriers when the energy is greater than or equal to the bandgap of the semiconductor, as illustrated in Figure 1.5. The charge generation comes in pairs, one electron in the conduction band and one hole in the valence band. These charges, on successful separation and migration from the bulk to the surface of a semiconductor, interacts with the adsorbed molecules (water and oxygen) to generate reactive species such as •OH and $O_2^{\bullet -}$ [20, 21]. This process can be utilized for water splitting, in which H_2 and O_2 gas are generated, or for the transformation of molecules into various products, such as the mineralization of pollutants into CO_2 and H_2O [15, 22]. Remarkably, the process does not require any artificial environment and takes place at room temperature and normal pressure, requiring only oxygen in the atmosphere, and light energy [15]. The reaction equations commonly involved in degradation of dye pollutants using semiconductor photocatalysts are described as follows [23, 24].

$$Photocatalyst + h\nu \rightarrow h^+ + e^- \quad (1.1)$$

$$O_2 + e^- \rightarrow O_2^{\bullet -} \quad (1.2)$$

$$O_2^{\bullet -} + e^- + 2H^+ \rightarrow H_2O_2 \quad (1.3)$$

$$O_2^{\bullet -} + H_2O_2 \rightarrow \bullet OH + OH^- + O_2 \quad (1.4)$$

$$e^- + H_2O_2 \rightarrow \bullet OH + OH^- \quad (1.5)$$

$$h^+ + OH^- \rightarrow \bullet OH \quad (1.6)$$

$$h^+ + H_2O \rightarrow H^+ + \bullet OH \quad (1.7)$$

$$2 \bullet OH \rightarrow H_2O_2 \quad (1.8)$$

$$h^+ + O_2^{\bullet -} \rightarrow {}^1O_2 \quad (1.9)$$

$$\text{Dye} + h^+ \rightarrow \text{dye oxidized} \quad (1.10)$$

$$\text{Dye} + e^- \rightarrow \text{dye reduced} \quad (1.11)$$

$$\text{Dye} + \bullet O_2^- \text{ or } \bullet O_2H \text{ or } \bullet OH \rightarrow \text{Degraded products} \quad (1.12)$$

The revolutionary concept of semiconductor-based heterogeneous photocatalysis was pioneered by Honda and Fujishima in 1972, when they demonstrated the photochemical splitting of water into hydrogen and oxygen using TiO_2, marking a transformative breakthrough in the field [25]. This study sparked the quest for clean energy among researchers in the scientific community. The idea of producing hydrogen by using only water and solar energy was new and profound. In 1995, a paper was published with title "Artificial Photosynthesis: Solar Splitting of Water to Hydrogen and Oxygen" highlighted the significance of semiconductor photocatalysis [26]. Earlier, in 1978, α-Fe_2O_3 electrodes had been used for the photo-oxidation of water [27]. Thereafter, studies on water splitting increased substantially, and soon photocatalysis was also applied to the degradation of dye pollutants. For instance, a paper published by Lakshmi et a. in 1995 reported the use of TiO_2 for the photocatalytic degradation of methylene blue [28]. Subsequently, in 1996, SnO_2/TiO_2 composite systems were explored for their applicability in the photocatalytic degradation of a textile azo dye [29]. Later, in 1999, the degradation of textile dyes using TiO_2 and ZnO photocatalysts under solar light was investigated [30].

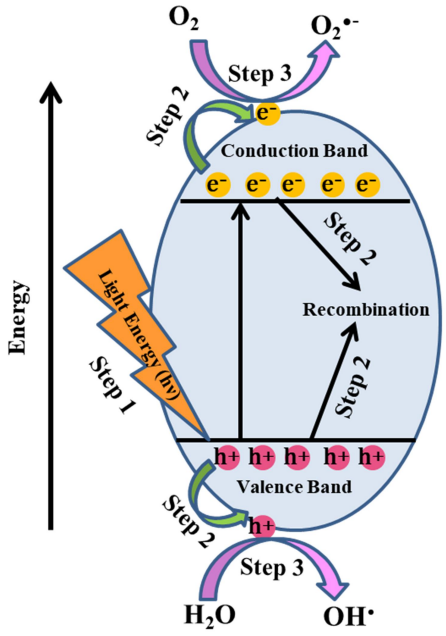

Figure 1.5. Illustration of semiconductor photocatalysis.

Numerous studies have been conducted, and research continues to explore novel and advanced materials for efficient photocatalysis to effectively degrade such pollutants. Figure 1.6 illustrates the number of studies on photocatalysis over the past decade.

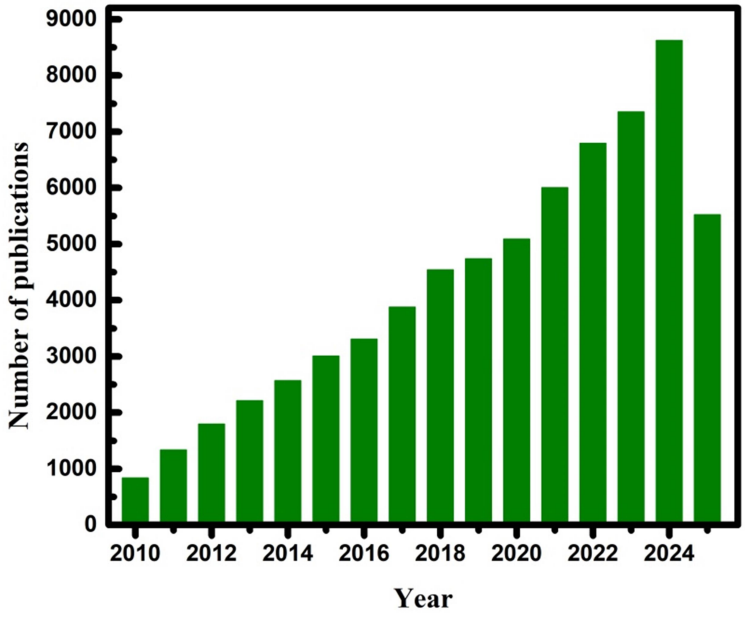

Figure 1.6. Bar chart showing the annual number of Scopus-indexed publications on photocatalysis from 2010 to 2025.

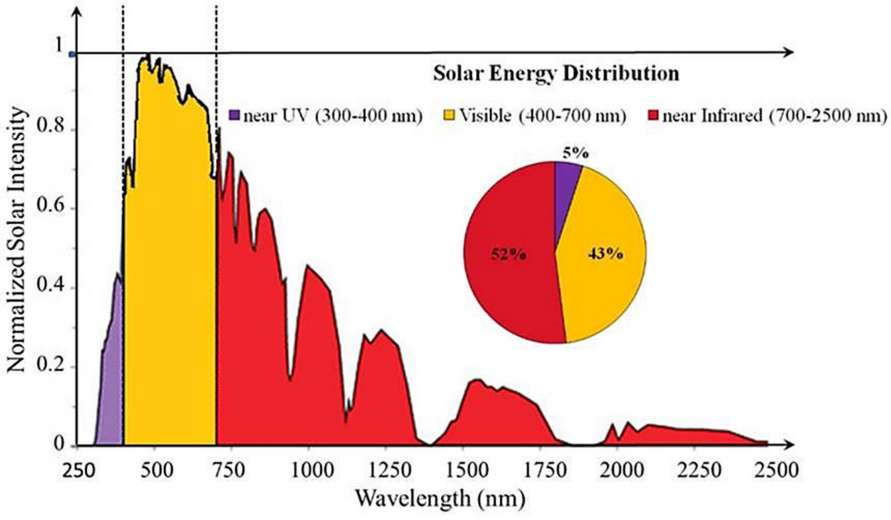

Figure 1.7. Solar spectrum showing the distribution of energy versus wavelength [31].

To achieve higher efficiency, photocatalysts must be capable of utilizing the visible light spectrum of solar energy while also meeting other essential criteria. This is because the solar spectrum consists of UV light (5%), visible light (43%) and near-infrared (NIR) light (52%), as illustrated in Figure 1.7. The spectrum shows that visible light has higher intensity than UV and NIR, accounting for 43% of solar radiation energy. Figure 1.8 depicts the global solar irradiance distribution for 2025, obtained from Solargis. The map clearly indicates that the solar irradiance in India is around 2000 KWh/m^2 annually, illustrating the country's abundance of intense solar energy. The solar irradiance measured across different parts of India on a daily basis is presented in Figure 1.9.

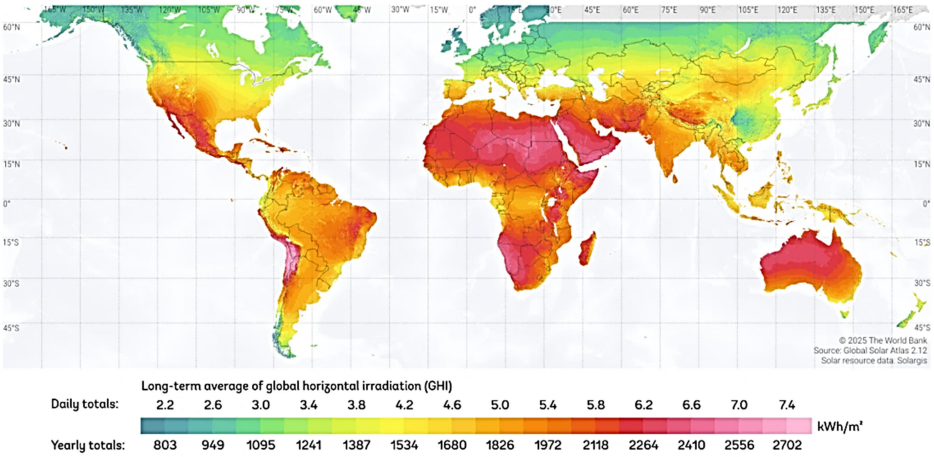

Figure 1.8. Map showing horizontal solar irradiance across different regions of the world [32]. (Solar resource map © 2021 Solargis)

The high bandgap nature of some of the widely used first generation semiconductor photocatalysts such as TiO_2, ZnO, and SnO_2, limits their absorption to UV light, prompting a shift in research focus toward developing visible light-active photocatalysts to efficiently harness a broader spectrum of solar energy. In 1998, $BiVO_4$ was reported to be applicable for O_2 evolution under visible light irradiation [33]. Similarly, silver halides (Ag/AgBr/TiO_2) were reported in 2006 as a visible light active photocatalyst [34]. In search of better and suitable photocatalysts, many studies were conducted and reported various photocatalysts such as Ag doped TiO_2, S-doped TiO_2, N-S-codoped TiO_2, WO_3, ZnO/Cu_2O, CuO, Cu_2O [35-40]. Since 2010, photocatalytic studies have increased significantly each year, and over the past two decades, numerous materials have demonstrated remarkable activity under both UV and visible-light irradiation. TiO_2

and ZnO have proven to be among the most effective photocatalysts despite their visible light insensitiveness, owing to their high chemical stability and biocompatibility. Between the two, TiO_2 is generally preferred, as it remains photocatalytically stable and resistant to photo-corrosion under light irradiation [11, 13, 16].

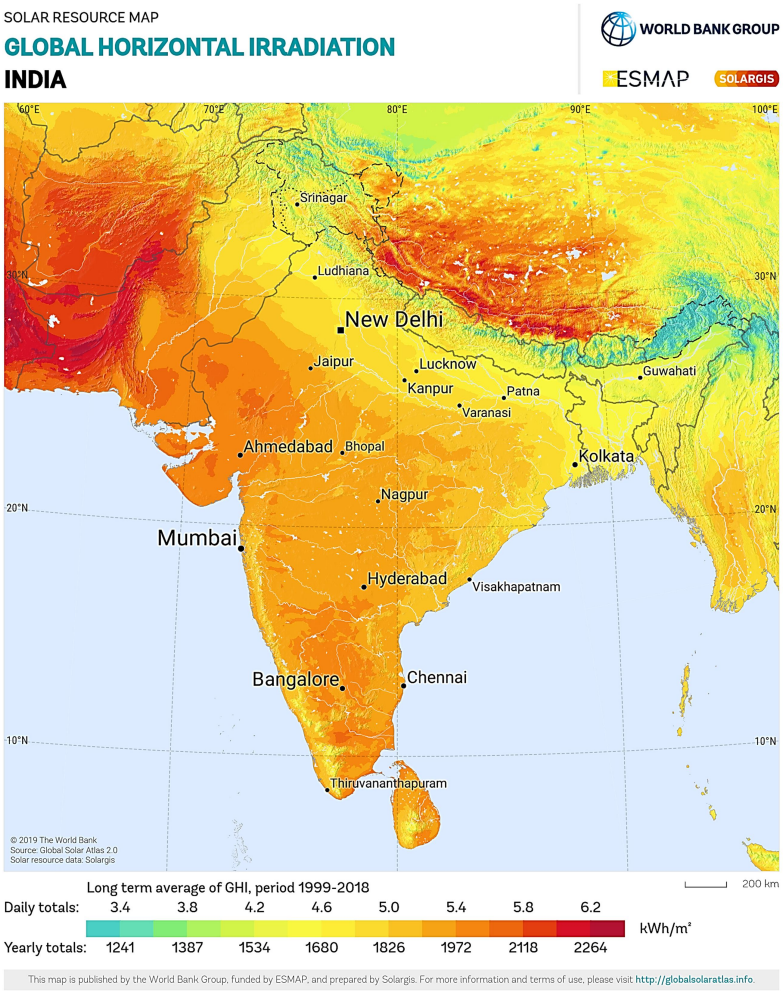

Figure 1.9. Illustration of horizontal solar irradiance levels across different regions of India [32]. (Solar resource map © 2021 Solargis)

Many photocatalytic studies used methylene blue (MB), rhodamine B (RhB), phenol as a model pollutant to discuss the effectiveness of a photocatalyst. MB is a widely used textile dye, known for its toxicity, carcinogenicity, and non-biodegradability, posing severe risks to human health, including respiratory distress, digestive and mental disorders, methemoglobinemia, and skin/eye irritation [41]. Similarly, RhB dye is considered harmful if ingested, and can cause skin, eye, and

respiratory irritation; it has also been proven to be carcinogenic, neurotoxic, and to exhibit reproductive toxic effects [42]. Likewise, phenol is regarded as a toxic and persistent pollutant that can generate carcinogenic byproducts, cause severe skin damage, metabolic disruption, and lead to fatal liver and kidney toxicity upon exposure [43].

Over the past two decades, extensive research has led to the development of various strategies and modifications aimed at enhancing the photocatalytic performance of semiconductor photocatalysts. The techniques such as doping, surface engineering, and defect engineering have been widely employed to optimize their structural, optical, and electronic properties. In addition to these approaches, researchers have introduced a new class of photocatalysts known as heterojunction photocatalysts, which integrate at least two semiconductors, offering significant advantages over conventional single-component photocatalysts. Categorically the key strategies are outlined below.

1.3.1. Doping and defects

Traditional benchmark photocatalysts such as TiO_2 and ZnO are wide bandgap semiconductors with energy gap values of 3.2 and 3.3 eV, respectively [21]. This implies that their photoactivity is limited to the UV region (< 387 nm) only, which constitutes to 3-5% of the solar spectrum [21, 44]. To improve their light absorption and extend it to the visible light range, doping is a commonly applied strategy. With a proper doping technique, the semiconductor not only shows improved light absorption but also exhibits reduced recombination compared to the parent semiconductor [45, 46]. Doping of metal and non-metal ions into lattices of wide bandgap semiconductors has been reported to modify the electronic structure of the semiconductors. The transition metal ions Cu, Co, Ni, Cr, Mn, Mo, Nb, V, Fe, Ru, Au, Ag, and Pt when used as dopants in TiO_2 and ZnO photocatalysts, introduces intra-band states close to the conduction band (CB) or valence band (VB) edge of the semiconductor as these transition metal ions possess redox energy states located just within the bandgap region of TiO_2 and ZnO [21]. The modified photocatalyst thus formed can therefore show photoactivity at sub-bandgap energies, absorbing visible light. Similarly, non-metal doping of semiconductors with N, S, C, B, P, I, and F ions creates localized states in the forbidden region of the material, allowing intra-band transitions under visible light illumination [21, 47]. In the case of metal doping, the metal ions also act as electron or hole traps,

thus affecting the steady state carrier concentration and in turn improving the photocatalytic degradation power. For instance, Fe^{3+}-TiO_2 exhibited excellent photoactivity on account of its partially filled electronic configuration, which behaves as shallow traps, in contrast to dopants having fully occupied electronic shells such as Mg^{2+}, Al^{3+}, Zn^{2+}, Ga^{3+}, Zn^{2+}, Nb^{5+}, Sn^{4+}, Sb^{5+}, and Ta^{5+}, which show lower photoactivity [48]. Likewise, iron-doped zinc oxide nanoflowers exhibited enhanced photocatalytic performance under visible light irradiation [49]. In one study, Park et al. synthesized metal doped TiO_2 photocatalysts using Ni, Co, Zn and Cu as dopants and observed that Cu-doped was the most promising for the photodegradation of methylene blue [50]. Similarly, Sangpour et al. investigated the photoactivity of TiO_2 doped with Ag, Au, and Cu, and found that Cu:TiO_2 outperformed all other counterparts [51]. Studies indicate that the photoactivity of metal ion-doped TiO_2 depends intricately and collectively on dopant concentration, energy states created in the lattice, electronic configuration, dopant distribution within the material, electron donor density, and incident light intensity [52, 53]. However, the drawbacks of metal doping arise from the same underlying physics that confer their advantage. Metal dopants tend to act as recombination centers due to the localized *d*-states they form in the bandgap region of TiO_2 [52]. This reduces the photodegradation rate by decreasing the number of electron-hole pairs reaching the catalyst surface. Metal dopants typically trap either electrons or holes depending on their impurity state in the host material, which can be disadvantageous since the complementary free charge carriers may swiftly recombine with the trapped charge carriers [48]. For example, Ni^{2+}-TiO_2 showed poor activity due to the high recombination occurring at the dopant level [54].

Consequently, non-metal doping has been explored as an alternative, with promising results. For example, C-TiO_2, prepared by hydrolyzing $TiCl_4$ with tetrabutylammonium hydroxide and calcining at 400 ºC for 1 hour, exhibited exceptional photocatalytic efficiency in breaking down 4-CP and remazol red under diffuse indoor daylight conditions [55]. Several studies on non-metal doped TiO_2, including N-, C-, and S-doped systems, have shown that the reduction in band-gap energy results from the interaction of N 2p, C 2p, and S 3p orbitals with the O 2p and Ti 3d states in the valence band of TiO_2 [21]. Research has shown that nitrogen doping is particularly advantageous due to its low ionization energy, formation of metastable

centers, stability, and atomic size, which is similar to that of oxygen [48, 56]. The presence of oxygen vacancies in N-doped TiO_2 can further enhance photocatalytic activity under visible light [21]. Nitrogen substitution influences both the surface structure and electronic properties of TiO_2, with the surface structure affecting charge carrier transfer, and the electronic properties determining the light absorption range and redox capabilities of the carriers [21, 57]. In essence, it was observed that the photocatalytic activity of non-metal-doped TiO_2 is primarily influenced by factors such as the dopant concentration, the energy level of the dopant within the lattice, its electron configuration, dopant distribution, the presence of oxygen vacancies on the lattice surface, and the intensity of incident light [46, 52]. However, non-metal doping also introduces drawbacks, such as defects in the oxide semiconductor, including oxygen vacancies, which can serve as recombination sites. The number of defects generally increases with dopant concentration, which may lead to a gradual reduction in the photocatalytic efficiency [46]. Therefore, an optimal dopant level must be determined for each photocatalyst system to achieve enhanced visible light absorption and photocatalytic activity while maintaining an acceptable defect density. Moreover, for doping to be considered successful, the crystal structure of host semiconductor oxide, such as TiO_2 or ZnO, must remain intact [46]. The primary challenges with non-metal doping include achieving uniform dopant distribution, identifying electronic states induced by dopants, ensuring doping stability under reaction conditions, and preserving the material's redox capabilities post doping [46]. Regardless of the dopant type: metal or non-metal, factors such as the dopant selection, its amount, and doping procedure must be precisely controlled to achieve the desired outcome. In particular, non-metal doping requires careful management of surface states and composition before and after doping to enhance the performance of the photocatalyst [46]. Other factors influencing the structure and degradation performance of the doped photocatalysts include the nature of pollutant, irradiation power, excitation wavelength, and more [48].

Nevertheless, doping often introduces defects, such as oxygen vacancies and other point defects, into semiconductors. Thus, the positive effects observed during doping are not solely due to the dopants themselves but are largely attributed to the defects created in the host semiconductor. These defects play a crucial role in altering the semiconductor's properties, particularly with respect to photocatalytic activity.

Consequently, defect engineering has emerged as a vital strategy for improving the photocatalytic performance of wide bandgap semiconductors and extending their light absorption into the visible range. The types of defects reported to influence photocatalytic activity are: point defects, line defects, planar defects, and volume defects [58]. Defect-rich photocatalytic materials can be fabricated through two main approaches: (i) introducing defects into pre-formed host nanomaterials via post-treatment processes such as hydrogen reduction, high temperature calcination, and vacuum deoxidation [59], or (ii) generating defects during the nanocrystal growth phase of the synthesis process [58]. The former approach is more widely employed than the latter. In post-treatment methods, only surface defects-such as vacancies, voids, and lattice disorders-are introduced due to the limited penetration depth of reactivity in pre-formed crystals. In contrast, synthesis-based methods enable the creation of bulk defects and other kinds of defects depending on the growth kinetics of nanocrystals.

A photocatalyst with bulk defects can benefit when such defects modify the band structure of the semiconductor to extend its light absorption to longer wavelengths [58]. On the other hand, surface defects may enhance photocatalytic performance by acting as highly active sites for catalysis [58]. The most common defects are oxygen vacancies, which have been reported in metal oxide semiconductor photocatalysts including TiO_2 [60], ZnO [61], WO_3 [62], Bi_2WO_6 [63], BiOCl [64], $BiPO_4$ [65], BiO_2 [66], and $SrTiO_3$ [67]. In many cases, vacancies and self-doped ions coexist in a crystal as a consequence of charge compensation involving positive and negative ions [58]. Unlike conventional doping, such vacancy-induced self-doping requires no incorporation of foreign elements. For instance, in N-doped TiO_2, nitrogen atoms act as foreign dopants that occupy interstitial sites of TiO_2 or substitute O sites at high concentration [68]. This produces point defects in the crystal system, resulting in a modified semiconductor photocatalyst composition. In contrast, line defects do not alter the composition of the photocatalyst. They are simply dislocations around which lattice atoms reorder in a new direction [58]. Reported examples include edge dislocations in TiO_2 and ZnO and screw dislocations in Cu_2O [69] , ZnO [70], and Ag_3PO_4 [71].

The weaker bonding at defect sites leads to a smaller energy separation between bonding and antibonding orbitals compared to the valence and conduction band states. This gives rise to electronic states within the bandgap, which either reduce the bandgap

energy or act as midgap states that facilitate electron photoexcitation, thereby extending light absorption range [58]. For instance, hydrogen-reduced blue TiO_2 (R-TiO_2) demonstrated enhanced light absorption at longer wavelengths compared to pristine TiO_2 (P-TiO_2) [72]. Hydrogen treatment introduced oxygen vacancies on the surface and subsurface, generating shallow and deep Ti(III) sub-bandgap states just below the conduction band. These defect states facilitated both defect-to-conduction band transitions and valence band-to-defect transitions. As a result, interband transitions allowed photoexcitation of R-TiO_2 by photons with energies lower than its bandgap, thereby improving visible-light photocatalytic activity.

The formation of midgap states due to vacancies has also been reported as a key factor in extending light absorption in ZnO, Bi_2WO_6, BiOCl, $BiPO_4$, $SrTiO_3$, and $La(OH)_3$ [58], all of which exhibit oxygen vacancies. Besides introducing midgap states, vacancies can also reduce the bandgap of semiconductors, further enhancing light absorption for photocatalysis. Such bandgap narrowing has been reported in oxygen-deficient TiO_2 [73], WO_3 [74], and vanadium-deficient $BiVO_4$ [75].

Defect-induced electronic states additionally affect charge carrier dynamics by enabling relaxation pathways. Both surface defects (trap states or surface states) and bulk defects influence electron-hole separation and transfer. For example, reducing the bulk-to-surface defect ratio in TiO_2 improves charge separation and photocatalytic efficiency [76]. However, bulk defects typically trap holes, leading to recombination with electrons, while surface defects may trap holes to react with pre-adsorbed donors, thereby promoting separation [77]. If trapped charges are not consumed promptly, surface defects may instead act as recombination sites. Thus, only with proper engineering can surface vacancies enhance charge migration, separation, and catalytic reactions, ultimately boosting photocatalytic activity [60]. In ZnO, bulk defects generally decrease photocatalytic efficiency, highlighting the importance of defect control. For instance, ball milling ZnO increased bulk defects, which lowered UV photocatalytic activity, whereas subsequent annealing reduced these defects and restored performance [78]. The bulk defects introduced new energy levels within the ZnO bandgap that served as recombination centers for electron-hole pairs. Similarly, Kong et al. used scanning tunneling microscopy (STM) to differentiate surface from subsurface defects, showing that samples with a lower bulk-to-surface defect ratio exhibited higher

photocatalytic efficiency [76] and increased photocurrent generation [77]. Thus, while defects can enhance photocatalytic activity in certain cases, they often hinder it by shortening charge carrier lifetimes, increasing recombination rates, and reducing crystallinity [77]. Excessive defects may trigger unwanted back reactions, further lowering performance. Additionally, managing defects becomes increasingly complex in multi-component hybrid photocatalysts, due to the structural challenges involved [58]. Ideally, defects in one component should not negatively influence the others, and simultaneous control over bulk, surface, and interfacial defects is required. However, current synthesis methods are generally limited to controlling only one defect parameter, such as structure, concentration, or location [58]. Moreover, characterization techniques have not advanced as rapidly as synthesis methods, creating obstacles in understanding defect-related photocatalytic mechanisms. For example, precise mapping of defect distribution and concentration remains difficult, and methods for quantifying certain defect types- especially those that do not affect composition or valence states, are still lacking [58]. Therefore, the intricate relationship between defect formation and photocatalytic activity demands deeper investigation and continues to present a promising avenue for research [60].

1.3.2. Heterojunction and surface engineering

For a photocatalyst to exhibit good activity under visible light, it must possess a suitably narrow bandgap, typically in the range of 1.7 to 3.1 eV. Simultaneously, achieving high redox potential requires that the CB of a material lies more negative and the VB more positive than the redox potentials of water. Reconciling both criteria within a single photocatalyst is often challenging; hence, the strategic integration of two or more semiconductors, forming a heterojunction with appropriately aligned band edge positions is widely employed to enhance photocatalytic efficiency [79]. Moreover, a significant limitation of single-component and doped photocatalysts is the rapid recombination of photogenerated charge carriers, which severely hampers their photocatalytic performance [80]. This drawback can be effectively mitigated through the construction of heterojunctions, wherein two distinct semiconductors are coupled to form n-n, n-p, or p-p type junctions, facilitating enhanced charge separation and prolonged carrier lifetimes [81, 82]. For instance, Liang et al. demonstrated that incorporating a Pt co-catalyst into a TiO_2/NiO p–n heterojunction significantly enhanced

both photocatalytic hydrogen evolution activity and operational stability [81]. Similarly, a Cu_2O–BiOI isotype p-p heterojunction has been shown to substantially boost visible light driven photoelectrochemical performance for non-enzymatic H_2O_2 sensing applications [83]. Heterojunction photocatalysts can also be prepared using a metal and a semiconductor, in which case a Schottky junction or ohmic contact is formed when the work function of the metal is higher or lower than that of semiconductor, respectively [81, 82].

The unique feature of heterojunctions is the formation of band bending at the interface between two dissimilar materials. This band bending induces an internal electric field across the junction, which plays a crucial role in promoting efficient charge carrier separation and suppressing the recombination of photogenerated electron-hole pairs. As a result, carriers generated in proximity to the junction are swiftly driven apart, thereby enhancing overall photocatalytic performance [82, 84]. The nature of band bending at a heterojunction interface can be significantly influenced by various interfacial properties, such as the presence of surface dipoles or defect states that act as charge traps. Additionally, factors like particle size, particular arrangement, and morphology play vital roles in modulating band alignment and the extent of band bending [80]. A study by Zhao et al. reported a reduction in charge recombination through the formation of a heterojunction between the {110} and {001} facets of BiOCl nanoplates [85]. The facet ratio was found to be crucial in determining photocatalytic activity. Similarly, by anchoring AgBr-Ag nanoparticles onto the exposed {010} facets of $BiVO_4$ microplates, a facet heterojunction was constructed, which exhibited enhanced photocatalytic bacterial inactivation [86]. These findings demonstrate how engineered band alignment at specific crystal facets can optimize charge separation and surface reactivity.

Based on the possible energy band alignments and resulting band bending at the interface, heterojunctions are generally classified into three types: Type I (straddling gap), Type II (staggered gap), and Type III (broken gap), as illustrated in Figure 1.10.

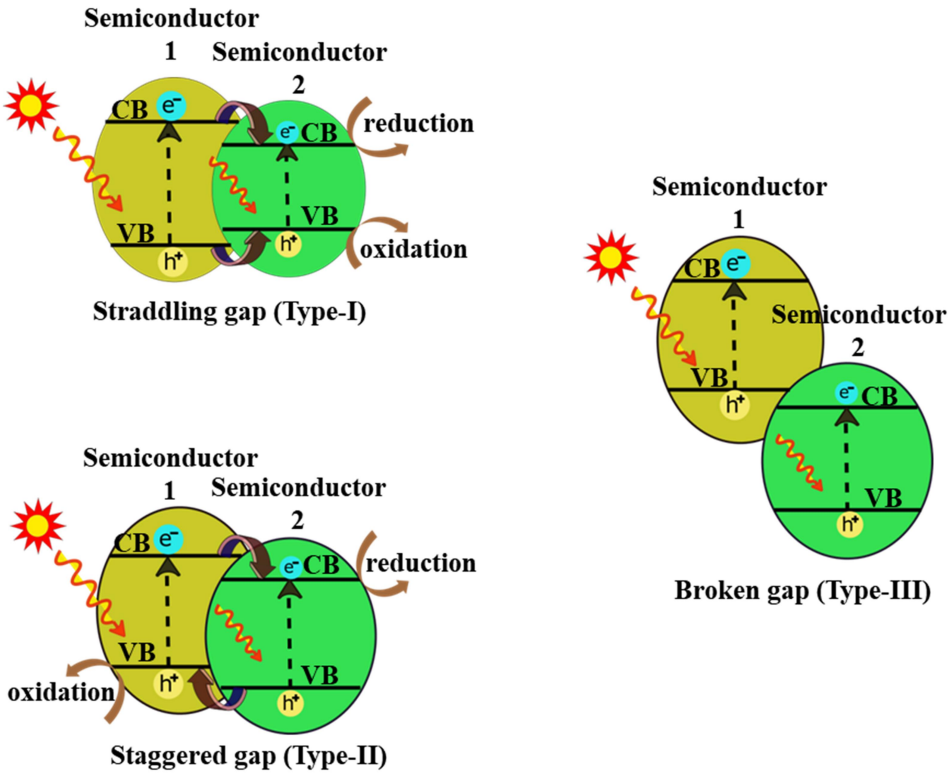

Figure 1.10. Classification of different types of heterojunctions.

A Type I heterojunction is formed when the CB and VB edges of the narrower bandgap semiconductor lie entirely within the corresponding CB and VB levels of the wider bandgap semiconductor [81]. This configuration facilitates the spatial confinement of both electrons and holes within the low bandgap material. Consequently, if the CB and VB of the low bandgap semiconductor do not align with the redox potentials required for the generation of reactive oxygen species (ROS) from water and oxygen, the photocatalyst will exhibit poor photocatalytic efficiency. A Type II heterojunction offers a more favorable architecture for photocatalysis, in which the CB and VB of one semiconductor lie at higher energies than those of the other, respectively [81]. In this configuration, electrons excited in the semiconductor with the higher CB position migrate to the semiconductor with the lower CB position, while holes generated in the semiconductor with the lower VB position transfer to the one with the higher VB position. As a result, effective charge separation is achieved, with electrons and holes moving in opposite directions. The efficiency of Type II heterojunctions is well-documented in the literature, with numerous studies reporting high photocatalytic

activity [87-90]. A Type III heterojunction is characterized by a discontinuous band structure in which the CB of one semiconductor lies below the VB position of the other. This unique alignment results in an overlap between the CB and VB edges across the interface, enabling direct band-to-band tunnelling (BTBT) of charge carriers [91]. In such systems, electrons can tunnel from the VB of one semiconductor directly into the CB of the adjacent semiconductor. However, Type-III heterojunctions do not support effective electron-hole migration and separation, limiting their applicability for enhancing charge carrier separation [92]. It is thus evident that the Type II heterojunction is the most effective traditional heterojunction for enhancing photocatalytic activity, owing to its favorable structure that facilitates spatial separation of electron-hole pairs. Showing even greater efficiency, sub-types of Type II heterojunctions, known as Z-scheme and S-scheme, have also been reported [81].

In a Z-scheme photocatalyst, electrons transfer from the CB of one semiconductor to the VB of another via an electron mediator, resulting in a larger potential difference between the reduction and oxidation sites compared to conventional heterojunctions. This expanded energy gap makes Z-scheme photocatalysts highly effective for redox reactions, including water splitting. Building on this concept, direct Z-scheme systems have been developed, in which electrons from the lower-lying CB of one semiconductor directly recombine with holes from the higher-lying VB of another without the need for external mediators such as redox couples or conductive bridges [80]. This direct charge recombination mechanism not only preserves strong redox potentials but also simplifies photocatalyst design, improving both efficiency and stability. To highlight its distinct characteristics and its ability to overcome the inherent limitations of traditional Z-scheme photocatalysts, Xu et al. redefined this class of systems as the S-scheme [79]. Clearly, heterojunction photocatalysts- particularly Z-scheme and S-scheme designs- represent superior architectures among Type II heterojunctions. The efficacy of heterojunctions can be further improved by optimizing several factors, including surface modifications which ensures the intimate contact between components (necessary for effective charge separation and the formation of an inbuilt electric field at the interface), the type of semiconductivity (n-type or p-type), as well as suitable work functions and Fermi levels [81, 82, 84]. Morphological variations, such as the difference between nanocrystals and nanowires of the same material, also influence photocatalytic activity

by affecting crystal facet-dependent reactivity or structural sensitivity [80]. Facets with higher surface energy, although thermodynamically less stable, can be obtained through precise optimization of synthesis conditions [93]. Overall, heterojunction photocatalysts hold great promise and can be further advanced through precise surface engineering, doping or modification with co-catalysts. A notable strategy involves the incorporation of noble metals, which can induce localized surface plasmon resonance (LSPR), a unique phenomenon that markedly enhances photoactivity.

1.3.3. Local surface plasmon resonance and plasmonic photocatalysts

Plasmonic photocatalysts are semiconductor materials integrated with plasmonic metals, which demonstrate enhanced photocatalytic activity through the utilization of surface plasmon resonance effects. Nanoparticles of noble metals such as Au, Ag, Cu, Pd, commonly referred to as plasmonic metals, support local surface plasmon resonance (LSPR), a light-induced phenomenon in which the free electrons of the nanoparticles respond to the time-varying electric field of incident light by undergoing collective oscillations within the localized region of the nanoparticle [94]. Resonance occurs when the wavelength of the incident light satisfies the conditions determined by the size, shape, surrounding medium, and electronic properties of metal particles [95]. LSPR is observed when the dimension of the plasmonic metal particle is smaller than the wavelength of the incident light and the electron mean free path in the material (Figure 1.11) [94]. Upon light irradiation, LSPR contributes to the photoactivity of plasmonic photocatalysts, which generally consist of at least two components: the plasmonic metal and a host semiconductor. To understand this concept, a uniform spherical particle can be considered as a representation of plasmonic metal nanoparticle under plane-wave light illumination as illustrated in Figure 1.12. Let the diameter of this sphere be R, characterized by a complex dielectric constant ε(ω), where ω is a complex function of angular frequency. Moreover, the sphere is assumed to be embedded in a non-magnetic, homogeneous, non-absorbing, and infinitely extended medium characterized by a dielectric constant ε_m. Under these circumstances, the electric field of the incident light is expressed as $\vec{E} = E_0 e^{-j\omega}\ \hat{x}$, where E_0 is the amplitude, $\hat{x}$ is the unit vector in the x direction and t is the time [96]. When the radiation strikes the sphere, the electric field $\vec{E}$ drives the free electrons within it to move in accordance with field's strength and direction. This motion is set into collective oscillation upon continuous irradiation

because the incident electric field changes its magnitude and direction with time. During oscillation, there exists a moment when the electrons are displaced toward one side of the sphere rendering that region negatively charged, while the diametrically opposite side becomes relatively positive. Consequently, an oscillating dipole resonates with the phase of the electric field, provided the sphere size permits the collective oscillation of electrons at a particular angular frequency (ω). The electric field due to this oscillating dipole coincides with the incident $\vec{E}$ outside the sphere, and a highly intense, localized net electric field (near-field) is produced in the vicinity of the sphere due to the superposition of these fields, given by [96]

$$\vec{E}_{out} = \vec{E} + \frac{1}{4\pi\varepsilon_0\varepsilon_m}\frac{1}{r^3}[3\hat{n}(\hat{n}.\vec{p}) - \vec{p}] \quad (1.13)$$

Here, $\vec{r} = r\,\hat{n}$ denotes the vector extending from the center of the sphere to the point where the field is being calculated. The term $\vec{E}$ corresponds to the electric field due to the incident electromagnetic wave, while the second term represents the radiation emitted by the point dipole $\vec{p}$. The $1/r^3$ dependence of the dipole contribution highlights that the field intensity diminishes rapidly as the distance from the centre of the sphere increases.

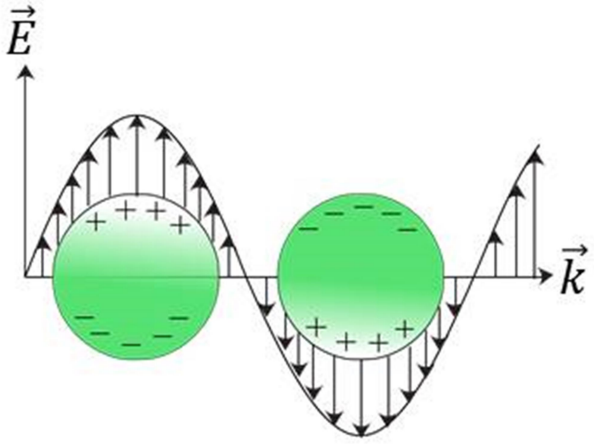

Figure 1.11. Local surface plasmon resonance on a spherical nanoparticle.

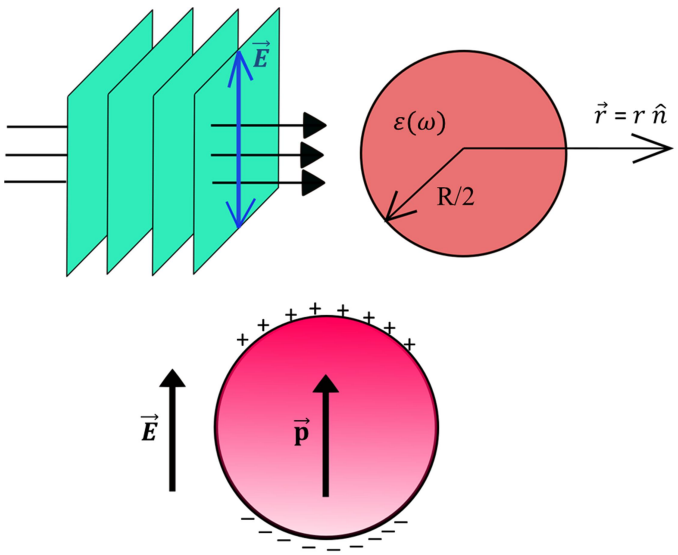

Figure 1.12. Illustration of a plane-wave light incident on a uniform spherical nanoparticle with diameter (R) and a complex frequency-dependent dielectric constant ε(ω). The external electric field $\vec{E}$ exerts a force on the free electrons within the nanosphere, resulting in the formation of an induced electric dipole.

The occurrence of LSPR in plasmonic photocatalyst enhances photocatalytic performance through various mechanisms, as elaborated in the subsequent discussion.

(i) Direct electron transfer (DET)

Plasmonic photocatalysts benefit from LSPR-driven phenomena, which arise when plasmonic metal nanostructures are in close contact with their host semiconductor counterparts [97]. A Schottky junction can form between plasmonic metal and semiconductor- for example, between Ag and TiO_2, when the work function of metal (Ag) nanoparticle is higher than that of semiconductor (TiO_2) nanoparticle. When LSPR is excited by the incident radiation on the plasmonic metal, whose surface may be exposed partially or entirely or covered but still accessible to radiation, the collective oscillation of conduction electrons of metal gives rise to plasmons [98]. The energy of these plasmons can then be transferred to electrons, enabling them to cross the metal-semiconductor Schottky barrier, and be injected into the conduction band of the host semiconductor [98]. These electrons are also known as hot electrons as they are highly energetic particles born out of surface plasmon decay (illustrated in Figure 1.13).

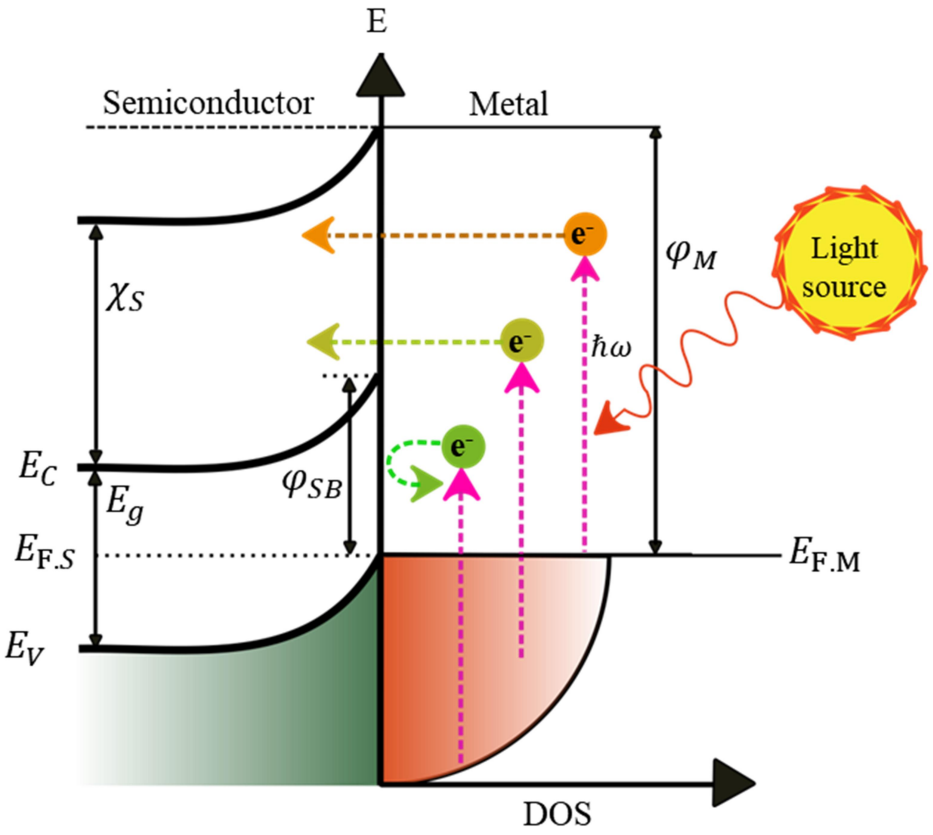

Figure 1.13. Schematic illustration of a semiconductor-metal Schottky junction with parabolic DOS. Light-induced hot electrons with energies exceeding the Schottky barrier are injected from the plasmonic metal into the conduction band of the semiconductor.

The hot electrons contribute to the population of available useful electrons of the photocatalyst, which participate in various redox reactions as described in equations (1.2 to 1.5), thereby boosting photocatalytic efficiency and performance [23]. The resonance wavelength of LSPR in plasmonic metal nanoparticles can be precisely tuned, irrespective of the semiconductor's response to incident radiation, by strategically optimizing parameters such as the size, and shape of the metal nanostructures. The photocatalytic role of the semiconductor counterpart is still retained though, including providing suitable band edge positions for redox reactions essential for efficient photocatalysis, facilitating charge separation via the Schottky barrier, offering a dielectric environment, contributing stability, laying out active sites, and providing a larger surface area for dye adsorption [96, 98].

(ii) Plasmon induced resonant energy transfer

Plasmonic photocatalysts are not solely dependent on the DET mechanism for enhanced performance. Even in the absence of close contact between the plasmonic metal and the semiconductor, they can harness an alternative LSPR-mediated mechanism known as plasmon-induced resonant energy transfer (PIRET) [97]. In this mechanism, electrons in the valence band of the semiconductor are promoted to the conduction band through near-field electromagnetic interaction. This interaction arises between the oscillating dipole of the LSPR active metal and the inter-band transition dipole of the semiconductor (displayed in Figure 1.14). Valence electrons in the semiconductor that lack insufficient energy to jump to the conduction band, even under light irradiation, can acquire the necessary excitation energy through PIRET. PIRET therefore enables their promotion to the conduction band, allowing them to actively participate in redox reactions and thereby enhance photocatalytic efficiency. In essence, LSPR dipole relaxation induces the generation of electron-hole pairs within the semiconductor [99]. PIRET-driven enhancement in the activity of the plasmonic photocatalyst is governed by two critical factors: the spatial separation between the plasmonic metal and the semiconductor, and the spectral overlap between the LSPR absorption band and the band edge of the semiconductor [99]. PIRET has been observed to occur for photocatalytic systems such as TiO_2-Au bilayer [100], Ag@SiO_2@CdS–Au [101], Ag@Cu_2O core-shell nanoparticles [99], and Au@SiO_2@Cu_2O nanoparticles [97], where there is an overlapping of SPR bands of the noble metal and the absorption band of the corresponding semiconductor counterpart. However, the efficiency of PIRET decreases as the separation distance between the metal and semiconductor increases, as observed in the core-shell structure of Ag@SiO_2@CdS. In this system, increasing the distance between the Ag NP core and the CdS shell resulted in a significant reduction in PIRET efficiency.

(iii) Local electromagnetic field enhancement

The near field, characterized by a spatially non-uniform local electric field, exhibits exponential decay with increasing distance from the plasmonic surface, typically spanning only a few nanometers. A semiconductor positioned sufficiently close to the plasmonic metal can interact with this near field, facilitating the excitation of electron-hole pairs even in the absence of plasmon-induced resonance energy transfer

(PIRET) [102]. Consequently, the electron-hole pair generation rate in the semiconductor increases significantly, often by several orders of magnitude [103]. When two plasmonic metals are brought into close proximity, separated by just a few nanometers, their interaction induces coupling effects that create highly localized regions known as 'hot spots' within the narrow gap [101, 104]. These hot spots exhibit an extraordinary enhancement of the electromagnetic field, with electric field intensities reaching up to 1000 times that of the incident field [95]. Plasmonic photocatalysts, when carefully designed, can harness this localized electromagnetic field enhancement (LEMF) effect to dramatically boost electron-hole pair generation, thereby substantially enhancing overall photocatalytic activity (Figure 1.14).

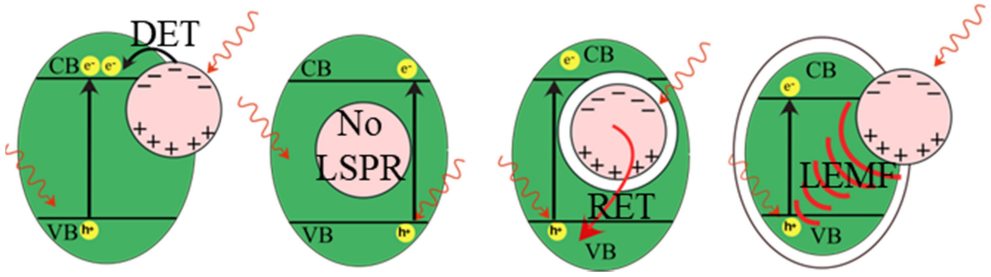

Figure 1.14. Mechanisms of charge separation in various photocatalytic nanostructures.

The aforementioned three effects arising due to LSPR significantly improve the performance of plasmonic photocatalysts compared to their non-plasmonic counterparts. However, to maximize the efficiency of plasmonic photocatalysis, it is crucial to optimize the photocatalyst's design by carefully addressing the factors influencing LSPR. The size of the plasmonic metal nanostructure as well as its shape greatly dictates the LSPR features. This dependency of LSPR on size and shape should be properly utilized to significantly improve the light-harnessing capability of the photocatalyst. The size dependence of LSPR is reflected upon the extinction spectra of plasmonic metal nanoparticles and on the intensity of the near-field. For nanoparticles with radii smaller than ~30 nm, absorption dominates over scattering due to their size being significantly smaller than the incident wavelength [105]. Scattering is only prominent as the particle size increases to be comparable to or larger than the wavelength [106]. In contrast to absorption and scattering cross-sections, surface plasmon-enhanced localized field intensity increases with decreasing nanoparticle size as observed in various studies

[107]. At a resonance wavelength of 410 nm, the electric field (E-field) enhancement for spherical Ag nanoparticles smaller than 20 nm was reported to be less than 200 times, while increasing the radius to 90 nm reduced the E-field enhancement to 25 times, caused by the increased radiative damping of LSPR [108]. In terms of resonant wavelength, larger particles exhibit red-shifted absorption spectra due to electrodynamic phase retardation, while smaller nanoparticles (< 5 nm) experience electron spill-out, reducing their plasmon energy, to cause red-shifted spectra again. For very small nanoparticles (< 3 nm), quantum confinement causes a blue shift, as the increased energy level separation requires higher energy for plasmon excitation. This trend was studied by Xiang et al. in which they used time-dependent orbital-free density functional theory (TD-OFDFT) to obtain the optical absorption trend for Na particles [109]. As the particle size increases, it is possible to separate the associated charges by less energetic incident radiation, allowing the collective oscillation of electrons to take place at lower frequency, causing a red-shift of the resonance peak. This behavior has been observed in Ag nanospheres and nanocubes. For the nanospheres, the dipolar resonance peak red-shifted from 400 to 450 nm as their diameter increased, while similar size-dependent shifts were observed in nanocubes with increasing edge length [110, 111]. For other shapes such as ellipsoids, nanorods, and cylindrical disks, the same behaviour was observed as their aspect ratio increased. Another size-dependent behaviour of LSPR is its influence on the number of plasmon modes that can be excited within a single nanoparticle. By varying the nanoparticle size relative to the incident wavelength, different plasmon modes can be activated [112, 113]. When the particle size is significantly smaller than the wavelength of the incident light, the dipole plasmon mode dominates. As the particle size approaches the wavelength, higher-order modes such as quadrupole and octupole emerge. These modes resonate with varying phases depending on the particle's internal spatial position, resulting from the spatial variation of electromagnetic field across the nanostructure [113]. The presence of multiple modes can broaden the extinction spectrum [112]. Moreover, for nanoparticles smaller than the electron mean free path, electromagnetic surface scattering can further broaden the plasmon resonance. As with shape, a single plasmonic metal element can display varying extinction spectra depending on its morphological features. Studies have shown that lowering symmetry in nanoparticles increases the number of resonances. For

example, nanobars and nanorods, with their limited symmetry, exhibit multiple resonances as polarization occurs along two distinct axes: the longer and shorter axes of nanobar. This produces two distinct peaks in the extinction spectrum, indicative of two distinct resonant wavelengths [114, 115]. The shorter wavelength peak corresponds to the transverse resonance, indicating that higher energy is required for polarization along this axis [116]. In contrast, a spherical nanoparticle requires the same energy for resonance regardless of the polarization direction, resulting in a single peak in the absorbance spectrum at a specific wavelength [117]. Shape also influences the intensity of the plasmonic resonance peak. Symmetries that allow greater charge separation facilitates stronger dipole formation and higher peak intensities compared to shapes lacking such features [118]. Additionally, nanostructures with sharp corners exhibit a notable shift in the plasmonic resonance peak towards longer wavelengths relative to rounded nanostructures of similar size [118, 119]. This is due to the fact that sharp corners facilitate effective charge separation, leading to a reduction in the restoring force required for the oscillation of the charges. This distinctive phenomenon has been reported in various structures, including truncated Ag triangular nanoplates, truncated cubes, and truncated octahedra [118, 120].

Besides tuning the plasmonic resonance wavelength of metal nanostructures, it is equally important to ensure compatibility between the plasmonic metal and the semiconductor counterpart. This not only affects the LSPR absorption features due to the dielectric environment but also determines photocatalytic efficiency. The energy harnessed by plasmons is transferred to available electrons based on the density of states (DOS) distribution within the conduction band of the nanostructure [98]. By optimizing the DOS distribution in the plasmonic material and appropriately adjusting the Schottky barrier, electronic states near the Fermi energy can be selectively excited [121]. Using compatible semiconductors such as TiO_2, known for its excellent electron-accepting properties owing to its high DOS in the conduction band, supports rapid electron injection from the plasmonic counterpart [98]. Another crucial parameter for efficient plasmonic photocatalysis is the optimal loading of plasmonic nanoparticles, as their concentration directly influences light absorption, charge transfer dynamics, and overall catalytic performance. For instance, the Au-NiOx nanocomposite demonstrated the highest photocatalytic efficiency at 11 wt.% Au across various film thicknesses [23].

Similarly, an optimal hydrogen production rate of 130 $mmol \cdot g^{-1} \cdot h^{-1}$ was achieved by incorporating 0.9 mL of Au satellite solution into the $Ag@SiO_2@CdS$ nanocomposite [101]. In Ag/Bi_2WO_6 composites, increasing Ag content beyond 1.0 wt.% reduced photocatalytic performance, attributed to the excess Ag or Au nanoparticles acting as recombination centers that facilitated electron-hole pair recombination [122]. Another study revealed that mesoporous TiO_2 with 5 wt.% Ag loading showed the best photocatalytic activity for degrading methylene blue and phenol under simulated sunlight [123].

Therefore, to explore highly efficient and advanced photocatalytic systems, the subsequent section delves into the strategic selection of suitable materials essential for the rational design and fabrication of high-performance plasmonic photocatalysts.

1.4. Potential materials for photocatalysis

1.4.1 Plasmonic materials

Among the noble metals, Ag (silver) and Au (gold) are the most commonly used plasmonic materials for studies associated with plasmonics. Au is known for its biocompatibility and for exhibiting versatile nanostructures. It exhibits interband transitions below 500 nm, making it well-suited for LSPR in the visible range above 500 nm [94]. In contrast, Ag is significantly more cost-effective than Au and exhibits the highest quality factor among all known noble metals, including Cu, Al, Pt, Li, and Pd, due to its exceptionally strong plasmon resonance with minimal damping [94]. Additionally, silver exhibits strong plasmonic resonance across the entire visible spectrum, making it highly suitable for visible-light-driven photocatalysis [124]. Similarly, lithium (Li) also demonstrates a broad plasmonic response in the visible range with commendable plasmonic strength, however, its high chemical reactivity significantly limits its practical application in plasmonics. Studies report that Ag can form a wide range of nanostructures with diverse sizes and morphologies. Numerous synthesis strategies, including facile chemical methods with high yield, have been developed to fabricate these Ag nanostructures efficiently [94, 118, 125]. Silver is comparatively less reactive than metals like lithium (Li) and less toxic than palladium (Pd). Moreover, both Pd and platinum (Pt) exhibit very low quality factors, making them unsuitable for plasmonic applications [94]. Copper (Cu) could be a promising alternative due to its cost-effectiveness and optical properties; however, its limited range

of reported nanostructures and high susceptibility to oxidation hinder practical use. Additionally, its interband transitions occur below 600 nm. Aluminum (Al), while demonstrating strong plasmonic activity, is primarily effective in the UV region and offers limited tunability in terms of nanostructure design [94, 124]. In terms of cost, the plasmonic metals Pt, Au, and Pd are relatively more expensive than Ag, Cu and Al [94].

1.4.2. Semiconductor materials

The selection and optimization of suitable semiconductors are pivotal for advancing photocatalytic technologies, as their intrinsic properties directly govern charge carrier generation and participations in the chemical reactions. Focused investigation in this area is essential to develop next-generation photocatalysts capable of addressing pressing environmental and energy challenges. The suitability and performance of semiconductor photocatalysts are evaluated based on numerous factors such as bandgap energy, charge carrier dynamics, stability, surface activity, and ease of synthesis. Semiconductor photocatalysts are broadly classified into two categories based on their bandgap: wide bandgap and narrow bandgap materials. While narrow bandgap semiconductors are active under visible light, many suffer from suboptimal band edge alignment for effective photocatalysis, high band-to-band electron-hole recombination rate, and may exhibit poor photoactivity after subsequent uses [96, 126]. Wide bandgap semiconductor photocatalysts, such as TiO_2 and ZnO are pioneering materials in photocatalysis research. They are UV active and regarded as benchmark photocatalysts due to their stability and suitable band edge positions, which provide strong redox potentials [80, 81, 127]. TiO_2 is widely recognized for its non-toxic nature, excellent photostability, and strong resistance to chemical corrosion. It can also be synthesized relatively easily using well-established methods such as sol-gel, hydrothermal, and chemical vapor deposition techniques [128]. Likewise, zinc oxide (ZnO) offers high electron mobility and cost-effective synthesis, with a bandgap comparable to that of TiO_2 [128]. However, despite its ease of fabrication, ZnO faces notable limitations, including susceptibility to photocorrosion and poor activity under visible light irradiation [11]. In terms of structural tunability, TiO_2 exhibits three natural polymorphs (anatase, rutile, and brookite), each with distinct properties and stabilities that influence its photocatalytic behaviour [129]. This phase diversity provides greater flexibility in tailoring TiO_2 for specific applications compared to ZnO, which predominantly

crystallizes in the wurtzite phase and lacks similar phase versatility under ambient conditions [130]. Nickel oxide (NiO) is another promising metal oxide photocatalyst, valued for its excellent chemical stability and strong redox potential, which arises from the wide separation gap between its valence and conduction bands [131]. NiO nanostructures can be synthesized through various methods, including sol-gel, precipitation, solvothermal techniques, and thermal decomposition. Among these, thermal decomposition of nickel precursors, particularly nickel hydroxide ($Ni(OH)_2$), is the most commonly reported and widely adopted approach [131]. SnO_2 is an n-type semiconductor photocatalyst with a wide bandgap ranging from 3.6 to 4.0 eV, offering excellent chemical and thermal stability [132]. Similarly, CeO_2 exhibits considerable potential as a photocatalyst, featuring a bandgap of ~3.2 eV and notable redox properties [133]. These wide bandgap metal oxides can be effectively tailored for visible-light-driven photocatalytic applications by strategically modifying their optoelectronic properties and morpho-structural features.

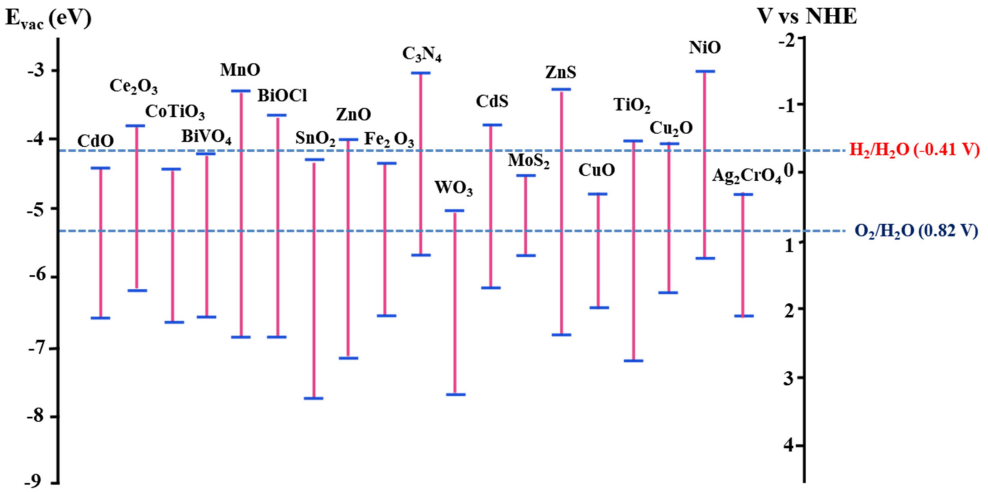

Figure 1.15. Band edge positions of some relevant semiconductor photocatalysts.

A wide range of other metal oxides with a relatively narrow bandgap such as WO_3, CuO, Cu_2O, $BiVO_4$, In_2O_3, SnO_2, and Ag_2CrO_4 also exhibit notable photocatalytic activity. One of the key parameters governing their effectiveness is the position of their conduction and valence band edges, which must align appropriately to facilitate the redox reactions for photocatalysis. These band edge positions are illustrated in Figure 1.15. However, most metal oxides suffer from limited stability and

are therefore often employed in heterojunctions or in combination with more robust semiconductors such as TiO_2 and ZnO to enhance structural and photocatalytic durability. Additionally, many of them require further investigation to optimize key parameters, including photocatalytic efficiency, reusability, and charge carrier dynamics. [80, 92, 134, 135]. Tungsten oxide (WO_3) is well-regarded for its remarkable stability in acidic environments and strong photooxidation capabilities. With a bandgap of approximately ~2.7 eV, it is responsive to visible light, enhancing its suitability for solar-driven applications. Moreover, WO_3 is relatively easy to synthesize using methods such as hydrothermal treatment, calcination, and precipitation techniques [126]. However, its photocatalytic efficiency is limited by the fast recombination of photogenerated charge carriers and poor hydrogen evolution activity, often requiring the addition of co-catalysts or coupling with other materials to enhance performance. Similarly, cupric oxide (CuO) and cuprous oxide (Cu_2O) are low-cost, earth-abundant, and non-toxic semiconductors that offer good chemical stability and versatility in nanostructure synthesis. Both exhibit p-type semiconductivity, with relatively narrow bandgaps of 1.2 eV for CuO and 2.0 eV for Cu_2O, making them promising for visible-light-driven photocatalysis [136]. Indium oxide (In_2O_3), on the other hand, is an n-type semiconductor oxide characterized by a direct optical bandgap ranging from 2.8 to 3.5 eV. Various synthesis methods, including solvothermal processes, template-assisted synthesis, hot injection techniques, laser ablation, and chemical vapor deposition, have been explored for producing In_2O_3 nanostructures. The study of In_2O_3-based nanostructured photocatalysts has gained significant attention due to their strong optical absorption in the UV-Vis spectrum, excellent stability in aqueous environments, adjustable physicochemical properties, and low toxicity [137]. Bismuth vanadate ($BiVO_4$) is also well explored attractive photocatalyst known for its visible light response owing to its bandgap value of 2.4 eV, non-toxicity, high stability, suitable valence band position, good dispersibility and corrosion resistance [138]. Hematite (α-Fe_2O_3) is a well-known photocatalyst for water splitting and methane production, with a narrow bandgap (2-2.3 eV) enabling absorption of ~40% of sunlight. Despite its high pH stability, it typically requires an external bias to effectively drive hydrogen evolution [95]. Notably, a group of Ag-based salts, such as Ag_3PO_4, Ag_2CO_3, $AgVO_3$, and $AgGaO_2$, has garnered significant attention for their capabilities in water splitting and

the degradation of organic pollutants in both air and aqueous solutions. Belonging to this group, Ag_2CrO_4 is a promising photocatalyst with a relatively narrow bandgap of approximately 1.75 eV, allowing it to strongly absorb visible light [139]. Recent studies have also focused on evaluating non-metal oxide photocatalysts such as g-C_3N_4 and CdS, owing to their strong visible light absorption and high photocatalytic efficiency. However, in terms of stability, these materials lag behind metal oxide photocatalysts. For instance, materials like CdS and ZnS are prone to degradation under photocatalytic conditions [80]. In addition, certain non-metal oxides, particularly Cd-based compounds, pose environmental hazards [140]. While materilas such as g-C_3N_4 and MoS_2 demonstrate excellent visible light absorption and hold promise for specific applications, metal oxides continue to dominate due to their superior stability, facile synthesis, environmental benignity, and cost-effectiveness [140]. The cost-effective metal oxide semiconductors are commonly based on elements from the 3d transition metal series such as Ti, Fe, Co, Ni, Cu, and Zn [141, 142]. These elements are earth-abundant, inexpensive, and widely available, making them attractive alternatives to noble metals or rare-earth elements [80]. Furthermore, their synthesis can typically be achieved through simple and scalable techniques such as sol–gel, hydrothermal, solvothermal, co-precipitation, and solid-state reactions, which are relatively low-cost and energy-efficient. These advantages make metal oxides more suitable for scalable and long-term photocatalytic applications, particularly for the treatment of industrial effluents.

Although the photocatalysts discussed above exhibit several promising properties, they often lack versatility and tunability, and typically require further modification. Unlike TiO_2, which has been extensively studied and optimized, many of these materials offer limited scope for improvement, particularly through bandgap engineering. As a result, they are frequently combined with TiO_2, ZnO, or other stable metal-oxides in heterojunction systems, or sensitized with noble metals, to enhance their photocatalytic performance and advance the development of next-generation photocatalysts [92].

1.5. Objectives and summary of thesis

Thus, in accordance with the aforementioned hierarchy in photocatalyst development, and with the aim of enhancing their efficiency, this thesis meticulously delineates and rigorously executes the following objectives.

(i) To prepare efficient solar light active heterojunction photocatalyst by plasmonic nanoparticle sensitization.

(ii) Fabrication of multi-junction photocatalytic system for enhancing its performance.

(iii) Development of viable photocatalyst through bandgap engineering and surface modification.

(iv) Study of the effect of size and shape of plasmonic nanostructures on the photocatalytic activity of a host material.

(v) Optimization of the various parameters of the host semiconductor and co-catalysts to obtain maximum efficiency.

The primary motivation behind undertaking these objectives stems from the urgent need to address the limitations of existing photocatalytic materials and to develop innovative solutions for escalating environmental challenges, particularly water pollution. To execute this, the thesis comprises seven chapters that systematically and comprehensively address the aforementioned objectives. **Chapter 2** presents a comprehensive account of the experimental procedures, including the synthesis methodologies employed to achieve the research objectives, mathematical formulations used for calculating key parameters, relevant chemical reaction equations, and detailed characterization techniques along with the analytical evaluation methods of the synthesized photocatalysts. **Chapter 3** details the experimental efforts directed toward designing a multi-junction photocatalyst with tailored bandgaps. The rationale behind this approach stems from the superior charge separation efficiency observed in heterojunction systems over single component semiconductors, as well as the bandgap narrowing effect introduced by doping. **Chapter 4** extends the work of the preceding chapter by incorporating plasmonic silver (Ag) into the multi-junction framework. This modification was aimed at leveraging plasmonic effects to further enhance photocatalytic performance. The chapter reports the successful fabrication of a hybrid system combining heterojunction and plasmonic components. Detailed analyses of the

optical, structural, morphological, and chemical characteristics are discussed. **Chapter 5** focuses on the development of another plasmon-enhanced heterojunction photocatalyst. This system was specifically designed to explore the benefits of various plasmon-induced energy transfer mechanisms on photocatalytic activity. **Chapter 6** investigates the role of plasmonic nanoparticles morphology in photocatalysis in titania-based systems, each integrated with differently shaped nanoparticles of the same metal. This chapter examines how particle shape influences performance, along with the systematic optimization of crucial parameters related to both the semiconductor matrix and the co-catalyst. The outcomes provide insights into the interplay between nanoparticle geometry and photocatalytic efficiency. **Chapter 7**, the concluding chapter, encapsulates the successful completion of the research objectives outlined at the outset of the thesis. It highlights the key findings from each experimental chapter and discusses their broader implications, particularly in the context of energy and environmental applications. The chapter also outlines potential directions for future work, emphasizing the significance of the current study.

References

1. E.F. Adolph, The metabolism and distribution of water in body and tissues, Physiol. Rev. 13 (1933) 336-371.
2. A. Gonsioroski, V.E. Mourikes, J.A. Flaws, Endocrine disruptors in water and their effects on the reproductive system, Int. J. Mol. Sci. 21 (2020) 1929
3. J. Gray, W. Shear, Early life on land, Am. Sci. 80 (1992) 444.
4. A. Porowski, Mineral and thermal waters, in: J.W. LaMoreaux (Ed.), Environmetal Geology, Springer, New York, 2019, pp. 149-181.
5. M. Salman, S. Jahan, S. Kanwal, F. Mansoor, Recent advances in the application of silica nanostructures for highly improved water treatment: a review, Environ. Sci. Pollut. Res. 26 (2019) 21065-21084.
6. L. Schweitzer, J. Noblet, Water contamination and pollution, in: B. Török, T. Dransfield (Eds.), Green Chemistry, Elsevier, 2018, pp. 261-290.
7. S. Dasgupta, X. Peng, S. Chen, J. Li, M. Du, Y.-H. Zhou, G. Zhong, H. Xu, K. Ta, Toxic anthropogenic pollutants reach the deepest ocean on Earth, Geochem. Perspect. Lett. 7 (2018) 22-26.

8. S. Kato, Y. Kansha, Comprehensive review of industrial wastewater treatment techniques, Environ. Sci. Pollut. Res. 31 (2024) 51064-51097.
9. N. Raghavendra, Drinking water contamination and its solving approaches: a comprehensive review of current knowledge and future directions, Water Air Soil Pollut. 235 (2024) 639.
10. B. Otto, L. Schleifer, Domestic water use grew 600% over the past 50 years, https://www.wri.org/insights/domestic-water-use-grew-600-over-past-50-years, 2020.
11. U.G. Akpan, B.H. Hameed, Parameters affecting the photocatalytic degradation of dyes using TiO_2-based photocatalysts: a review, J. Hazard. Mater. 170 (2009) 520-529.
12. M. Saeed, M. Muneer, A.U. Haq, N. Akram, Photocatalysis: an effective tool for photodegradation of dyes—a review, Environ. Sci. Pollut. Res. 29 (2022) 293-311.
13. A.O. Ibhadon, P. Fitzpatrick, Heterogeneous photocatalysis: recent advances and applications, Catalysts 3 (2013) 189-218.
14. A. Asghar, A.A.A. Raman, W.M.A.W. Daud, Advanced oxidation processes for in-situ production of hydrogen peroxide/hydroxyl radical for textile wastewater treatment: a review, J. Clean. Prod. 87 (2015) 826-838.
15. S.N. Ahmed, W. Haider, Heterogeneous photocatalysis and its potential applications in water and wastewater treatment: a review, Nanotechnology 29 (2018) 342001.
16. M.R. Al-Mamun, S. Kader, M.S. Islam, M.Z.H. Khan, Photocatalytic activity improvement and application of UV-TiO_2 photocatalysis in textile wastewater treatment: A review, J. Environ. Chem. Eng. 7 (2019) 103248.
17. J.T. Richardson, Principles of catalyst development, Springer, New York, 2013.
18. N. Serpone, A.V. Emeline, Suggested terms and definitions in photocatalysis and radiocatalysis, Int. J. Photoenergy 4 (2002) 91-131.
19. R.K. Nath, M.F.M. Zain, M. Jamil, An environment-friendly solution for indoor air purification by using renewable photocatalysts in concrete: A review, Renew. Sustain. Energy Rev. 62 (2016) 1184-1194.
20. C. Belver, J. Bedia, A. Gómez-Avilés, M. Peñas-Garzón, J.J. Rodriguez, Semiconductor photocatalysis for water purification, in: S. Thomas, D. Pasquini,

S.Y. Leu, D. A. Gopakumar (Eds.), Nanoscale materials in water purification, Elsevier, 2019, pp 581-651.

21. M.R.D. Khaki, M.S. Shafeeyan, A.A.A. Raman, W.M.A.W. Daud, Application of doped photocatalysts for organic pollutant degradation—a review, J. Environ. Manag. 198 (2017) 78-94.
22. N. Fajrina, M. Tahir, A critical review in strategies to improve photocatalytic water splitting towards hydrogen production, Int. J. Hydrog. Energy 44 (2019) 540–577.
23. D. Fragua, J. Noguera-Gomez, P.J. Rodríguez-Canto, L.M. Valencia, M. De La Mata, M. Herrera, S.I. Molina, R. Abargues, Au–NiO_x nanocomposite for hot electron-assisted plasmonic photocatalysis, J. Mater. Chem. C 8 (2020) 9885-9897.
24. M. Cho, H. Chung, W. Choi, J. Yoon, Linear correlation between inactivation of E. coli and OH radical concentration in TiO_2 photocatalytic disinfection, Water Res. 38 (2004) 1069-1077.
25. A. Fujishima, K. Honda, Electrochemical photolysis of water at a semiconductor electrode, Nature 238 (1972) 37-38.
26. A.J. Bard, M.A. Fox, Artificial photosynthesis: solar splitting of water to hydrogen and oxygen, Acc. Chem. Res. 28 (1995) 141-145.
27. J.H. Kennedy, K.W. Frese, Photooxidation of water at α-Fe_2O_3 electrodes, J. Electrochem. Soc. 125 (1978) 709.
28. S. Lakshmi, R. Renganathan, S. Fujita, Study on TiO_2-mediated photocatalytic degradation of methylene blue, J. Photochem. Photobiol. A: Chem. 88 (1995) 163-167.
29. K. Vinodgopal, I. Bedja, P.V. Kamat, Nanostructured semiconductor films for photocatalysis. Photoelectrochemical behavior of SnO_2/TiO_2 composite systems and its role in photocatalytic degradation of a textile azo dye, Chem. Mater. 8 (1996) 2180-2187.
30. B. Neppolian, S. Sakthivel, B. Arabindoo, M. Palanichamy, V. Murugesan, Degradation of textile dye by solar light using TiO_2 and ZnO photocatalysts, J. Environ. Sci. Health Part A 34 (1999) 1829-1838.
31. S. Escobedo, H. de Lasa, Photocatalysis for air treatment processes: Current technologies and future applications for the removal of organic pollutants and viruses, Catalysts 10 (2020) 966.

32. Solar resource maps & GIS data, https://solargis.com/resources/free-maps-and-gis-data, 2025
33. A. Kudo, K. Ueda, H. Kato, I. Mikami, Photocatalytic O_2 evolution under visible light irradiation on $BiVO_4$ in aqueous $AgNO_3$ solution, Catal. Lett. 53 (1998) 229-230.
34. C. Hu, Y. Lan, J. Qu, X. Hu, A. Wang, Ag/AgBr/TiO_2 visible light photocatalyst for destruction of azodyes and bacteria, J. Phys. Chem. B 110 (2006) 4066-4072.
35. N. Sobana, K. Selvam, M. Swaminathan, Optimization of photocatalytic degradation conditions of Direct Red 23 using nano-Ag doped TiO_2, Sep. Purif. Technol. 62 (2008) 648-653.
36. T. Ohno, T. Mitsui, M. Matsumura, Photocatalytic activity of S-doped TiO_2 photocatalyst under visible light, Chem. Lett. 32 (2003) 364-365.
37. F. Wei, L. Ni, P. Cui, Preparation and characterization of N-S-codoped TiO_2 photocatalyst and its photocatalytic activity, J. Hazard. Mater. 156 (2008) 135-140.
38. M. Hepel, S. Hazelton, Photoelectrocatalytic degradation of diazo dyes on nanostructured WO_3 electrodes, Electrochim. Acta 50 (2005) 5278-5291.
39. C. Xu, L. Cao, G. Su, W. Liu, H. Liu, Y. Yu, X. Qu, Preparation of ZnO/Cu_2O compound photocatalyst and application in treating organic dyes, J. Hazard. Mater. 176 (2010) 807-813.
40. V. Scuderi, G. Amiard, S. Boninelli, S. Scalese, M. Miritello, P.M. Sberna, G. Impellizzeri, V. Privitera, Photocatalytic activity of CuO and Cu_2O nanowires, Mater. Sci. Semicond. Process. 42 (2016) 89-93.
41. I. Khan, K. Saeed, I. Zekker, B. Zhang, A.H. Hendi, A. Ahmad, S. Ahmad, N. Zada, H. Ahmad, L.A. Shah, T. Shah, I. Khan, Review on methylene blue: its properties, uses, toxicity and photodegradation, Water 14 (2022) 242
42. R. Jain, M. Mathur, S. Sikarwar, A. Mittal, Removal of the hazardous dye rhodamine B through photocatalytic and adsorption treatments, J. Environ. Manag. 85 (2007) 956-964.
43. A. Abd Gami, M.Y. Shukor, K.A. Khalil, F.A. Dahalan, A. Khalid, S.A. Ahmad, Phenol and its toxicity, J. Environ. Microbiol. Toxicol. 2 (2014) 11-23.
44. W. Jiang, S. Bai, L. Wang, X. Wang, L. Yang, Y. Li, D. Liu, X. Wang, Z. Li, J. Jiang, Y. Xiong, Integration of multiple plasmonic and co-catalyst nanostructures

on TiO_2 nanosheets for visible-near-infrared photocatalytic hydrogen evolution, Small 12 (2016) 1640-1648.

45. N.U. Saqib, R. Adnan, I. Shah, A mini-review on rare earth metal-doped TiO_2 for photocatalytic remediation of wastewater, Environ. Sci. Pollut. Res. 23 (2016) 15941-15951.
46. R. Marschall, L. Wang, Non-metal doping of transition metal oxides for visible-light photocatalysis, Catal. Today 225 (2014) 111-135.
47. M. Szkoda, K. Siuzdak, A. Lisowska-Oleksiak, Non-metal doped TiO_2 nanotube arrays for high efficiency photocatalytic decomposition of organic species in water, Phys. E: Low-Dimens. Syst. Nanostructures 84 (2016) 141-145.
48. L.G. Devi, R. Kavitha, A review on non metal ion doped titania for the photocatalytic degradation of organic pollutants under UV/solar light: Role of photogenerated charge carrier dynamics in enhancing the activity, Appl. Catal. B: Environ. 140 (2013) 559-587.
49. S. Yi, J. Cui, S. Li, L. Zhang, D. Wang, Y. Lin, Enhanced visible-light photocatalytic activity of Fe/ZnO for rhodamine B degradation and its photogenerated charge transfer properties, Appl. Surf. Sci. 319 (2014) 230-236.
50. J.Y. Park, K.I. Choi, J.H. Lee, C.H. Hwang, D.Y. Choi, J.W. Lee, Fabrication and characterization of metal-doped TiO_2 nanofibers for photocatalytic reactions, Mater. Lett. 97 (2013) 64-66.
51. P. Sangpour, F. Hashemi, A.Z. Moshfegh, Photoenhanced degradation of methylene blue on cosputtered M:TiO_2 (M = Au, Ag, Cu) nanocomposite systems: a comparative study, J. Phys. Chem. C 114 (2010) 13955-13961.
52. M. Nasirian, Y.P. Lin, C.F. Bustillo-Lecompte, M. Mehrvar, Enhancement of photocatalytic activity of titanium dioxide using non-metal doping methods under visible light: a review, Int. J. Environ. Sci. Technol. 15 (2018) 2009-2032.
53. W. Choi, A. Termin, M.R. Hoffmann, The role of metal ion dopants in quantum-sized TiO_2: correlation between photoreactivity and charge carrier recombination dynamics, J. Phys. Chem. 98 (2002) 13669-13673.
54. L.G. Devi, S.G. Kumar, Influence of physicochemical–electronic properties of transition metal ion doped polycrystalline titania on the photocatalytic degradation

of Indigo Carmine and 4-nitrophenol under UV/solar light, Appl. Surf. Sci. 257 (2011) 2779-2790.

55. S. Sakthivel, H. Kisch, Daylight photocatalysis by carbon-modified titanium dioxide, Angew. Chem. Int. Ed. 42 (2003) 4908-4911.
56. L. Bergamonti, G. Predieri, Y. Paz, L. Fornasini, P.P. Lottici, F. Bondioli, Enhanced self-cleaning properties of N-doped TiO_2 coating for Cultural Heritage, Microchem. J. 133 (2017) 1-12.
57. R. Asahi, T. Morikawa, T. Ohwaki, K. Aoki, Y. Taga, Visible-light photocatalysis in nitrogen-doped titanium oxides, Science 293 (2001) 269-271.
58. S. Bai, N. Zhang, C. Gao, Y. Xiong, Defect engineering in photocatalytic materials, Nano Energy 53 (2018) 296-336.
59. T.L. Thompson, J.T. Yates, TiO_2-based photocatalysis: surface defects, oxygen and charge transfer, Top. Catal. 35 (2005) 197-210.
60. X. Pan, M.Q. Yang, X. Fu, N. Zhang, Y.J. Xu, Defective TiO_2 with oxygen vacancies: synthesis, properties and photocatalytic applications, Nanoscale 5 (2013) 3601-3614.
61. S.A. Ansari, M.M. Khan, S. Kalathil, A. Nisar, J. Lee, M.H. Cho, Oxygen vacancy induced band gap narrowing of ZnO nanostructures by an electrochemically active biofilm, Nanoscale 5 (2013) 9238-9246.
62. G. Wang, Y. Ling, H. Wang, X. Yang, C. Wang, J.Z. Zhang, Y. Li, Hydrogen-treated WO_3 nanoflakes show enhanced photostability, Energy Environ. Sci. 5 (2012) 6180-6187.
63. J. Tian, Y. Sang, G. Yu, H. Jiang, X. Mu, H. Liu, A Bi_2WO_6-based hybrid photocatalyst with broad spectrum photocatalytic properties under UV, visible, and near-infrared irradiation, Adv. Mater. 25 (2013) 5075-5080.
64. H. Li, J. Li, Z. Ai, F. Jia, L. Zhang, Oxygen vacancy-mediated photocatalysis of BiOCl: reactivity, selectivity, and perspectives, Angew. Chem. Int. Ed. 57 (2018) 122-138.
65. Y. Lv, Y. Zhu, Y. Zhu, Enhanced photocatalytic performance for the $BiPO_{4-x}$ nanorod induced by surface oxygen vacancy, J. Phys. Chem. C 117 (2013) 18520-18528.

66. J. Li, X. Wu, W. Pan, G. Zhang, H. Chen, Vacancy-rich monolayer BiO_{2-x} as a highly efficient UV, visible, and near-infrared responsive photocatalyst, Angew. Chem. Int. Ed. 57 (2018) 491-495.
67. H. Tan, Z. Zhao, W.B. Zhu, E. N. Coker, B. Li, M. Zheng, W. Yu, H. Fan, Z. Sun, Oxygen vacancy enhanced photocatalytic activity of pervoskite $SrTiO_3$, ACS Appl. Mater. Interfaces 6 (2014) 19184-19190.
68. J. Wang, D.N. Tafen, J.P. Lewis, Z. Hong, A. Manivannan, M. Zhi, M. Li, N. Wu, Origin of photocatalytic activity of nitrogen-doped TiO_2 nanobelts, J. Am. Chem. Soc. 131 (2009) 12290-12297
69. S. Hacialioglu, F. Meng, S. Jin, Facile and mild solution synthesis of Cu_2O nanowires and nanotubes driven by screw dislocations, Chem. Commun. 48 (2012) 1174-1176.
70. S.A. Morin, S. Jin, Screw dislocation-driven epitaxial solution growth of ZnO nanowires seeded by dislocations in GaN substrates, Nano Lett. 10 (2010) 3459-3463.
71. J.D. Wang, J.K. Liu, C.X. Luo, Y. Lu, X.H. Yang, Silver phosphate crystal growth by screw dislocation driven of dynamic-template, Cryst. Growth Des. 13 (2013) 4837-4843
72. S.K. Cushing, F. Meng, J. Zhang, B. Ding, C.K. Chen, C.J. Chen, R.S. Liu, A.D. Bristow, J. Bright, P. Zheng, N. Wu, Effects of defects on photocatalytic activity of hydrogen-treated titanium oxide nanobelts, ACS Catal. 7 (2017) 1742-1748.
73. L. Li, J. Yan, T. Wang, Z.J. Zhao, J. Zhang, J. Gong, N. Guan, Sub-10 nm rutile titanium dioxide nanoparticles for efficient visible-light-driven photocatalytic hydrogen production, Nat. Commun. 6 (2015) 5881.
74. Y. Li, Z. Tang, J. Zhang, Z. Zhang, Defect engineering of air-treated WO_3 and its enhanced visible-light-driven photocatalytic and electrochemical performance, J. Phys. Chem. C 120 (2016) 9750-9763.
75. S. Gao, B. Gu, X. Jiao, Y. Sun, X. Zu, F. Yang, W. Zhu, C. Wang, Z. Feng, B. Ye, Y. Xie, Highly efficient and exceptionally durable CO_2 photoreduction to methanol over freestanding defective single-unit-cell bismuth vanadate layers, J. Am. Chem. Soc. 139 (2017) 3438-3445.

76. M. Kong, Y. Li, X. Chen, T. Tian, P. Fang, F. Zheng, X. Zhao, Tuning the relative concentration ratio of bulk defects to surface defects in TiO_2 nanocrystals leads to high photocatalytic efficiency, J. Am. Chem. Soc. 133 (2011) 16414-16417.
77. D. Maarisetty, S.S. Baral, Defect engineering in photocatalysis: formation, chemistry, optoelectronics, and interface studies, J. Mater. Chem. A 8 (2020) 18560-18604.
78. D. Chen, Z. Wang, T. Ren, H. Ding, W. Yao, R. Zong, Y. Zhu, Influence of defects on the photocatalytic activity of ZnO, J. Phys. Chem. C 118 (2014) 15300-15307.
79. Q. Xu, L. Zhang, B. Cheng, J. Fan, J. Yu, S-scheme heterojunction photocatalyst, Chem 6 (2020) 1543-1559.
80. A.B. Djurišić, Y. He, A. Ng, Visible-light photocatalysts: prospects and challenges, APL Mater. 8 (2020) 030903.
81. A. Balapure, J.R. Dutta, R. Ganesan, Recent advances in semiconductor heterojunctions: a detailed review of the fundamentals of photocatalysis, charge transfer mechanism and materials, RSC Appl. Interfaces 1 (2024) 43-69.
82. H. Wang, L. Zhang, Z. Chen, J. Hu, S. Li, Z. Wang, J. Liu, X. Wang, Semiconductor heterojunction photocatalysts: design, construction, and photocatalytic performances, Chem. Soc. Rev. 43 (2014) 5234-5244.
83. Y. Zhang, Q. Wang, D. Liu, Q. Wang, T. Li, Z. Wang, Cu_2O-BiOI isotype (pp) heterojunction: Boosted visible-light-driven photoelectrochemical activity for non-enzymatic H_2O_2 sensing, Appl. Surf. Sci. 521 (2020) 146434.
84. S.J. Moniz, S.A. Shevlin, D.J. Martin, Z.X. Guo, J. Tang, Visible-light driven heterojunction photocatalysts for water splitting–a critical review, Energy Environ. Sci. 8 (2015) 731-759.
85. H. Zhao, X. Liu, Y. Dong, Y. Xia, H. Wang, X. Zhu, Fabrication of a Z-scheme {001}/{110} facet heterojunction in BiOCl to promote spatial charge separation, ACS Appl. Mater. Interfaces 12 (2020) 31532-31541.
86. S. Bao, Z. Wang, J. Zhang, B. Tian, Facet-heterojunction-based Z-scheme $BiVO_4$ {010} microplates decorated with AgBr-Ag nanoparticles for the photocatalytic inactivation of bacteria and the decomposition of organic contaminants, ACS Appl. Nano Mater. 3 (2020) 8604-8617.

87. X. Ren, K. Wu, Z. Qin, X. Zhao, H. Yang, The construction of type II heterojunction of Bi_2WO_6/BiOBr photocatalyst with improved photocatalytic performance, J. Alloys Compd. 788 (2019) 102-109.
88. X. Jiang, M. Wang, B. Luo, Z. Yang, W. Li, D. Zhang, X. Pu, P. Cai, Magnetically recoverable flower-like Sn_3O_4/$SnFe_2O_4$ as a type-II heterojunction photocatalyst for efficient degradation of ciprofloxacin, J. Alloys Compd. 926 (2022) 166878.
89. H. Cui, S. Dong, K. Wang, M. Luan, T. Huang, Synthesis of a novel Type-II In_2S_3/Bi_2MoO_6 heterojunction photocatalyst: Excellent photocatalytic performance and degradation mechanism for Rhodamine B, Sep. Purif. Technol. 255 (2021) 117758.
90. Y. Wang, Q. Wang, X. Zhan, F. Wang, M. Safdar, J. He, Visible light driven type II heterostructures and their enhanced photocatalysis properties: a review, Nanoscale 5 (2013) 8326-8339.
91. N. Ferdous, M.S. Islam, J. Park, A resilient type-III broken gap Ga_2O_3/SiC van der Waals heterogeneous bilayer with band-to-band tunneling effect and tunable electronic property, Sci. Rep. 14 (2024) 12748.
92. J. Low, J. Yu, M. Jaroniec, S. Wageh, A.A. Al-Ghamdi, Heterojunction photocatalysts, Adv. Mater. 29 (2017) 1601694.
93. M. Ge, C. Cao, J. Huang, S. Li, Z. Chen, K.Q. Zhang, S.S. Al-Deyab, Y. Lai, A review of one-dimensional TiO_2 nanostructured materials for environmental and energy applications, J. Mater. Chem. A 4 (2016) 6772-6801.
94. M. Rycenga, C.M. Cobley, J. Zeng, W. Li, C.H. Moran, Q. Zhang, D. Qin, Y. Xia, Controlling the synthesis and assembly of silver nanostructures for plasmonic applications, Chem. Rev. 111 (2011) 3669-3712.
95. W. Hou, S.B. Cronin, A review of surface plasmon resonance-enhanced photocatalysis, Adv. Funct. Mater. 23 (2013) 1612-1619.
96. X. Zhang, Y.L. Chen, R.S. Liu, D.P. Tsai, Plasmonic photocatalysis, Rep. Prog. Phys. 76 (2013) 046401.
97. S.K. Cushing, J. Li, F. Meng, T.R. Senty, S. Suri, M. Zhi, M. Li, A.D. Bristow, N. Wu, Photocatalytic activity enhanced by plasmonic resonant energy transfer from metal to semiconductor, J. Am. Chem. Soc. 134 (2012) 15033-15041.

98. C. Clavero, Plasmon-induced hot-electron generation at nanoparticle/metal-oxide interfaces for photovoltaic and photocatalytic devices, Nat. Photon. 8 (2014) 95-103.
99. J. Li, S.K. Cushing, J. Bright, F. Meng, T.R. Senty, P. Zheng, A.D. Bristow, N. Wu, Ag@Cu_2O core-shell nanoparticles as visible-light plasmonic photocatalysts, ACS Catal. 3 (2013) 47-51.
100. F. Tan, T. Li, N. Wang, S.K. Lai, C.C. Tsoi, W. Yu, X. Zhang, Rough gold films as broadband absorbers for plasmonic enhancement of TiO_2 photocurrent over 400–800 nm, Sci. Rep. 6 (2016) 33049.
101. H. Ren, J.L. Yang, W.M. Yang, H.L. Zhong, J.S. Lin, P.M. Radjenovic, L. Sun, H. Zhang, J. Xu, Z.Q. Tian, J.F. Li, Core-shell-satellite plasmonic photocatalyst for broad-spectrum photocatalytic water splitting, ACS Mater. Lett. 3 (2020) 69-76.
102. H. Wang, T. You, W. Shi, J. Li, L. Guo, Au/TiO_2/Au as a plasmonic coupling photocatalyst, J. Phys. Chem. C 116 (2012) 6490-6494.
103. Z. Lou, Z. Wang, B. Huang, Y. Dai, Synthesis and activity of plasmonic photocatalysts, ChemCatChem 6 (2014) 2456-2476.
104. Z. Hu, Y. Mi, Y. Ji, R. Wang, W. Zhou, X. Qiu, X. Liu, Z. Fang, X. Wu, Multiplasmon modes for enhancing the photocatalytic activity of Au/Ag/Cu_2O core–shell nanorods, Nanoscale 11 (2019) 16445-16454.
105. R.S. Geonmonond, A.G. da Silva, T.S. Rodrigues, I.C. de Freitas, R.A. Ando, T.V. Alves, P.H. Camargo, Addressing the effects of size-dependent absorption, scattering, and near-field enhancements in plasmonic catalysis, ChemCatChem 10 (2018) 3447-3452.
106. H.F. Zarick, O. Hurd, J.A. Webb, C. Hungerford, W.R. Erwin, R. Bardhan, Enhanced efficiency in dye-sensitized solar cells with shape-controlled plasmonic nanostructures, ACS Photon. 1 (2014) 806-811.
107. M. Achermann, Exciton-plasmon interactions in metal−semiconductor nanostructures, J. Phys. Chem. Lett. 1 (2010) 2837-2843.
108. E. Hao, G.C. Schatz, Electromagnetic fields around silver nanoparticles and dimers, J. Chem. Phys. 120 (2004) 357-366.
109. H. Xiang, X. Zhang, D. Neuhauser, G. Lu, Size-dependent plasmonic resonances from large-scale quantum simulations, J. Phys. Chem. Lett. 5 (2014) 1163-1169.

110. C.M. Cobley, M. Rycenga, F. Zhou, Z.Y. Li, Y. Xia, Controlled etching as a route to high quality silver nanospheres for optical studies, J. Phys. Chem. C 113 (2009) 16975-16982.
111. J.J. Mock, M. Barbic, D.R. Smith, D.A. Schultz, S. Schultz, Shape effects in plasmon resonance of individual colloidal silver nanoparticles, J. Chem. Phys. 116 (2002) 6755-6759.
112. T. Kiba, K. Masui, Y. Inomata, A. Furumoto, M. Kawamura, Y. Abe, K.H. Kim, Control of localized surface plasmon resonance of Ag nanoparticles by changing its size and morphology, Vacuum 192 (2021) 110432.
113. S.L. Westcott, J.B. Jackson, C. Radloff, N.J. Halas, Relative contributions to the plasmon line shape of metal nanoshells, Phys. Rev. B 66 (2002) 155431.
114. B.J. Wiley, Y. Chen, J.M. McLellan, Y. Xiong, Z.Y. Li, D. Ginger, Y. Xia, Synthesis and optical properties of silver nanobars and nanorice, Nano Lett. 7 (2007) 1032-1036.
115. X. Huang, I.H. El-Sayed, W. Qian, M.A. El-Sayed, Cancer cell imaging and photothermal therapy in the near-infrared region by using gold nanorods, J. Am. Chem. Soc. 128 (2006) 2115-2120.
116. B.G. McMillan, L.E. Berlouis, F.R. Cruickshank, D. Pugh, P.F. Brevet, Transverse and longitudinal surface plasmon resonances of a hexagonal array of gold nanorods embedded in an alumina matrix, Appl. Phys. Lett. 86 (2005) 211912.
117. Y.W. Ma, Z.W. Wu, L.H. Zhang, J. Zhang, G.S. Jian, S. Pan, Theoretical study of the local surface plasmon resonance properties of silver nanosphere clusters, Plasmonics 8 (2013) 1351-1360.
118. B.J. Wiley, S.H. Im, Z.Y. Li, J. McLellan, A. Siekkinen, Y. Xia, Maneuvering the surface plasmon resonance of silver nanostructures through shape-controlled synthesis, J. Phys. Chem. B 110 (2006) 15666-15675.
119. Y. Wang, D. Wan, S. Xie, X. Xia, C.Z. Huang, Y. Xia, Synthesis of silver octahedra with controlled sizes and optical properties via seed-mediated growth, ACS Nano 7 (2013) 4586-4594.
120. J. Zeng, S. Roberts, Y. Xia, Nanocrystal-based time–temperature indicators, Chem.-Eur. J. 16 (2010) 12559-12563.

121. Z. Li, X. Meng, Recent development on palladium enhanced photocatalytic activity: a review, J. Alloys Compd. 830 (2020) 154669.
122. J. Li, Z. Guo, Z. Zhu, Ag/Bi_2WO_6 plasmonic composites with enhanced visible photocatalytic activity, Ceram. Int. 40 (2014) 6495-6501.
123. T. Liu, B. Li, Y. Hao, F. Han, L. Zhang, L. Hu, A general method to diverse silver/mesoporous–metal–oxide nanocomposites with plasmon-enhanced photocatalytic activity, Appl. Catal. B Environ. 165 (2015) 378-388.
124. E.L. Ru, P. Etchegoin, Principles of Surface–Enhanced Raman Spectroscopy: and Related Plasmonic Effects, Elsevier, Oxford, U.K, 2009.
125. X. Zheng, L. Zhu, A. Yan, X. Wang, Y. Xie, Controlling synthesis of silver nanowires and dendrites in mixed surfactant solutions, J. Colloid Interface Sci. 268 (2003) 357-361.
126. V. Dutta, S. Sharma, P. Raizada, V.K. Thakur, A.A.P. Khan, V. Saini, A.M. Asiri, P. Singh, An overview on WO_3 based photocatalyst for environmental remediation, J. Environ. Chem. Eng. 9 (2021) 105018.
127. A.N. Tuama, L.H. Alzubaidi, M.H. Jameel, K.H. Abass, M.Z.H. bin Mayzan, Z. N. Salman, Impact of electron–hole recombination mechanism on the photocatalytic performance of ZnO in water treatment: a review, J. Sol-Gel Sci. Technol. 110 (2024) 792-806.
128. S. Hernández, D. Hidalgo, A. Sacco, A. Chiodoni, A. Lamberti, V. Cauda, E. Tresso, G. Saracco, Comparison of photocatalytic and transport properties of TiO_2 and ZnO nanostructures for solar-driven water splitting, Phys. Chem. Chem. Phys. 17 (2015) 7775-7786.
129. D.R. Eddy, M.D. Permana, L.K. Sakti, G.A.N. Sheha, Solihudin, S. Hidayat, T. Takei, N. Kumada, I. Rahayu, Heterophase polymorph of TiO_2 (anatase, rutile, brookite, TiO_2(B)) for efficient photocatalyst: fabrication and activity, Nanomaterials 13 (2023) 704.
130. C.B. Ong, L.Y. Ng, A.W. Mohammad, A review of ZnO nanoparticles as solar photocatalysts: synthesis, mechanisms and applications, Renew. Sustain. Energy Rev. 81 (2018) 536-551.

131. F. Motahari, M.R. Mozdianfard, F. Soofivand, M. Salavati-Niasari, NiO nanostructures: synthesis, characterization and photocatalyst application in dye wastewater treatment, RSC Adv. 4 (2014) 27654-27660.
132. J.L.A. do Nascimento, L. Chantelle, I.M.G. dos Santos, A.L. Menezes de Oliveira, M.C.F. Alves, The influence of synthesis methods and experimental conditions on the photocatalytic properties of SnO_2: a review, Catalysts 12 (2022) 428.
133. E. Kusmierek, A CeO_2 semiconductor as a photocatalytic and photoelectrocatalytic material for the remediation of pollutants in industrial wastewater: a review, Catalysts 10 (2020) 1435.
134. S. Lettieri, M. Pavone, A. Fioravanti, L. Santamaria Amato, P. Maddalena, Charge carrier processes and optical properties in TiO_2 and TiO_2-based heterojunction photocatalysts: a review, Materials 14 (2021) 1645.
135. X. Gu, C. Li, S. Yuan, M. Ma, Y. Qiang, J. Zhu, ZnO based heterojunctions and their application in environmental photocatalysis, Nanotechnology 27 (2016) 402001.
136. S. Mosleh, M.R. Rahimi, M. Ghaedi, K. Dashtian, S. Hajati, Sonochemical-assisted synthesis of $CuO/Cu_2O/Cu$ nanoparticles as efficient photocatalyst for simultaneous degradation of pollutant dyes in rotating packed bed reactor: LED illumination and central composite design optimization, Ultrason. Sonochem. 40 (2018) 601-610.
137. K.K. Pawar, L.S. Chaudhary, S.S. Mali, T.S. Bhat, A.D. Sheikh, C.K. Hong, P.S. Patil, In_2O_3 nanocapsules for rapid photodegradation of crystal violet dye under sunlight, J. Colloid Interface Sci. 561 (2020) 287-297.
138. S. Lotfi, M.E. Ouardi, H.A. Ahsaine, A. Assani, Recent progress on the synthesis, morphology and photocatalytic dye degradation of $BiVO_4$ photocatalysts: a review, Catal. Rev. 66 (2024) 214-258.
139. D. Xu, S. Cao, J. Zhang, B. Cheng, J. Yu, Effects of the preparation method on the structure and the visible-light photocatalytic activity of Ag_2CrO_4, Beilstein J. Nanotechnol. 5 (2014) 658-666.
140. S.K. Loeb, P.J.J. Alvarez, J.A. Brame, E.L. Cates, W. Choi, J. Crittenden, D.D. Dionysiou, Q. Li, G. Li-Puma, X. Quan, D.L. Sedlak, T.D. Waite, P. Westerhoff, J.-H. Kim, The technology horizon for photocatalytic water treatment: sunrise or sunset?, Environ. Sci. Technol. 53 (2019) 2937-2947.

141. N. Ghosh, S. Das, G. Biswas, P.K. Haldar, Review on some metal oxide nanoparticles as effective adsorbent in wastewater treatment, Water Sci. Technol. 85 (2022) 3370-3395.

142. M.P. Browne, Z. Sofer, M. Pumera, Layered and two dimensional metal oxides for electrochemical energy conversion, Energy Environ. Sci. 12 (2019) 41-58.